

# Co-designing electronics with microfluidics for more sustainable cooling

*Remco van Erp, Reza Soleimanzadeh, Luca Nela, Georgios Kampitsis & Elison Matioli\**

*École Polytechnique Fédérale de Lausanne (EPFL)*

*(\*Corresponding author: [elison.matioli@epfl.ch](mailto:elison.matioli@epfl.ch) )*

1 Thermal management is one of the main challenges for the future of electronics [1]–[5].  
2 With the ever increasing rate of data generation and communication, as well as the  
3 constant push to reduce volume and costs of industrial converter systems, the power  
4 density of electronics rises [6]. Consequently, cooling has an increasingly large  
5 environmental impact [7], [8], and new technologies are needed to efficiently handle the  
6 heat in a sustainable and cost-effective way [9]. Embedding liquid cooling directly  
7 inside the chip is a promising approach for a more efficient thermal management [5],  
8 [10], [11]. However, even in state-of-the-art approaches, the electronics and cooling are  
9 treated separately, leaving the full energy-saving potential of embedded cooling  
10 untapped. Here we demonstrate that co-designing microfluidics and electronics into the  
11 same semiconductor substrate, to produce a monolithically-integrated manifold  
12 microchannel (mMMC) cooling structure, provides efficiency beyond the state-of-the-  
13 art. Our results show that heat fluxes exceeding  $1.7 \text{ kW/cm}^2$  can be cooled down using  
14 only  $0.57 \text{ W/cm}^2$  of pumping power. We observed an unprecedented coefficient of  
15 performance ( $>10^4$ ) for single-phase water-cooling of heat fluxes exceeding  $1 \text{ kW/cm}^2$ ,  
16 corresponding to a 50-fold increase compared to straight microchannels, as well as a  
17 remarkably high average Nusselt number of 16. The proposed cooling technology  
18 enables further miniaturization of electronics, potentially extending Moore's law and  
19 greatly reducing energy consumption worldwide. Furthermore, by removing the need  
20 for large external heat sinks, we demonstrate how this approach enables ultra-compact

21 **power converters integrated on a single chip, supporting the electrification trend of our**  
22 **society.**

23 Data centers, in the US alone, consume 24 TWh of electricity and 100 billion liters of water to  
24 satisfy their cooling demands [8], corresponding to the residential needs of a city of the size of  
25 Philadelphia [12]–[14]. Their environmental impact is expected to increase dramatically [9],  
26 accounting for 31% of the Ireland’s electricity demand by 2027 [15]. This development is  
27 accompanied by the constant push to reduce the size of semiconductor devices, which results  
28 in higher heat-fluxes that become increasingly challenging to cool down. A similar trend is  
29 observed in power electronics, as the electrification of our society demands more powerful,  
30 efficient and smaller energy conversion systems. Wide-band-gap semiconductors, such as  
31 gallium nitride (GaN), are promising candidates for this purpose [16]. These materials enable  
32 much-smaller dies than traditional semiconductors as well as the monolithic integration of  
33 power devices, supporting the miniaturization of complete power converters into a single chip  
34 [17]. However, to unlock its full potential, new strategies for sustainable cooling of high heat-  
35 flux applications are required.

36 Significant research efforts focus on improving the thermal path between the hot-spot and the  
37 coolant [12]. However, their heat extraction capability is fundamentally limited by the thermal  
38 resistance between the semiconductor die and packaging. Furthermore, relying on large heat  
39 sinks hinders the power density and integration, since devices cannot be densely packed.  
40 Bringing the coolant in direct contact with the device is an actively-investigated strategy to  
41 break this limit. For example, impinging coolant on a bare die [18], or etching micrometer-sized  
42 channels directly inside the device to turn the substrate into a heat-sink. The latter  
43 demonstrated state-of-the-art cooling performance by exploiting the much-improved heat  
44 transfer at the microscale [19]–[21]. The high pressure drop and large temperature gradients  
45 associated with these straight, parallel microchannels (SPMCs) were overcome by splitting the  
46 flow into multiple parallel sections, and distributing the coolant over these channels using  
47 manifolds [22]. Early investigations [23]–[26] and systematic numerical studies [27]–[30] of

48 manifold microchannel (MMC) heat sinks showed a significant reduction in pumping power  
49 requirements and thermal resistance compared to SPMCs. Excellent heat extraction has been  
50 demonstrated with copper microchannels [31], compact micro-fabricated multi-layer silicon  
51 structures [32]–[35], and by using additive manufacturing [36] [37]. However, in all these  
52 approaches, the heat sink and electronic structure and fabrication process are considered  
53 separately, either by integrating a simple resistive heater functioning as heat source, or by  
54 bonding the MMC structure to a commercial device [38]. This leaves the large potential of  
55 MMCs untapped. Improving the thermal coupling between the heat source and cooling was  
56 investigated for hot-spot mitigation [39]–[41], but remained unexplored for a complete device  
57 structure. Furthermore, despite the long history of MMC heat-sinks research, the increasing  
58 complexity and associated reliability concerns due to the multiple bonded layers required for  
59 coolant delivery have prevented its adoption in commercial devices.

60 In this work, we address these concerns by demonstrating a new paradigm for cooling and  
61 device design, in which a MMC heat-sink is designed and fabricated in conjunction with the  
62 electronics. This led to a novel *monolithically-integrated* manifold microchannel (mMMC) heat-  
63 sinks in a single-crystalline silicon substrate without the need for cumbersome bonding steps.  
64 Here the device design and heat-sink fabrication are combined within the same process, with  
65 buried cooling channels embedded right below the active area of the chip. Coolant impinging  
66 directly underneath the heat sources provides local and efficient heat extraction (Fig. 1a).  
67 Within this same substrate, manifold channels spread the liquid over the die (Fig. 1c) to obtain  
68 high temperature-uniformity and low pressure-drop, leading to a very low pumping-power  
69 consumption and vastly improved cooling performance. Since the electronics and microfluidics  
70 are fully coupled and aligned (Fig. 1b), this approach is denominated as *Microfluidic-electronic*  
71 *co-design*. We demonstrated this microfluidic-electronic co-design on GaN-on-Si, a low-cost  
72 platform promising for realizing high-power converters on a chip, comprising a few micrometer-  
73 thick GaN epilayer on a low-cost silicon substrate. The passive silicon substrate typically lacks  
74 functionality, but by turning it into an active cooling layer, it has the potential to extract extreme

75 heat fluxes, without the added cost of high-thermal conductivity substrates. Our results show  
76 that considering cooling as an integral part of device design can result in orders-of-magnitude  
77 improvement in cooling performance. The embedded-cooling approach is used to demonstrate  
78 a super-compact GaN-on-silicon integrated AC-DC converter, containing four power devices  
79 on the same microfluidic-cooled chip, yielding a power density of 25 kW/dm<sup>3</sup>. A simple multi-  
80 layered printed circuit board (PCB) was designed to direct the coolant flow into the  
81 semiconductor device.

## 82 **Co-design concept and fabrication**

83 Our proposed co-design approach, where each heat source is coupled to an individual buried  
84 cooling-channel serving as a local heat sink, is particularly interesting for lateral GaN power  
85 electronic applications. Typical source-drain spacing for high electron mobility transistors in  
86 >1kV applications matches the optimum dimensions for microchannel cooling of ~20 μm, [19],  
87 [42]–[44]. Therefore, we investigated a GaN-on-Si device structure in which liquid impinges  
88 directly onto the epilayer below each contact, ensuring minimum thermal resistance between  
89 the hot-spot and coolant. In this structure (Fig. 1a), the GaN epilayer provides the power  
90 electronics (Fig 1b), and the silicon functions as microchannel cooling and fluid-distribution  
91 network in a 3D arrangement (Fig 1c). Figure 1d illustrates the corresponding fabrication  
92 method. A staggered pattern of slits was formed in the Si by anisotropic deep-etch through  
93 narrow incisions in the AlGaN/GaN epilayer to achieve the desired microchannel depth. This  
94 pattern provided better structural integrity of the epilayer during fabrication compared to  
95 continuous slits. During the subsequent isotropic gas-etch, the channels widened and  
96 coalesced in the silicon substrate, while monitored through the transparent GaN epilayer using  
97 an in-situ optical etch-rate tracking. This two-step etching process provides independent  
98 control over channel width and depth, making it suitable to a wide range of contact pitches.  
99 The incisions were finally hermetically-sealed during the device metallization step. The  
100 methods section, as well as Extended data Fig. 1, explain the fabrication procedure in details.  
101 Figure 1e shows a scanning electron microscope (SEM) image of the device after the

102 metallization step with sealed channels. Because of the narrow incisions in the epilayer, the  
103 contacts do not require significant oversizing. The microchannels are in direct contact with the  
104 active area of the chip, thus providing excellent thermal coupling between the hot-spot and the  
105 cooling channel (Fig. 1f). Through micron-sized openings in the AlGaIn/GaN layer, 125  $\mu\text{m}$ -  
106 deep and 20  $\mu\text{m}$ -wide channels were realized in the silicon substrate (Fig. 1g,h).

107 A series of devices was fabricated with SPMCs with equal width and spacing of 100  $\mu\text{m}$ , 50  
108  $\mu\text{m}$  and 25  $\mu\text{m}$ , and a channel depth of 250  $\mu\text{m}$  in GaN-on-Si power devices, functioning as  
109 reference heat sinks (Fig. 2a) for evaluating the performance of the co-designed electronic-  
110 microfluidic mMMC devices. mMMC chips with 2, 4 and 10 inlet and outlet manifold channels  
111 and identical 20  $\times$  125  $\mu\text{m}$  microchannels were fabricated, referred to as 2x, 4x and 10x-  
112 manifold (Fig. 2b). Figure 2c shows a picture of the mMMC device with 10x-manifold, including  
113 a schematic (Fig 2d) to illustrate the flow path with coolant impinging directly onto the bottom  
114 of the GaN epilayer.

### 115 **Thermo-hydraulic evaluation**

116 A thermo-hydraulic analysis, using de-ionized water as a coolant, was performed on the 6  
117 cooling structures (Fig. 2a,b) to assess the cooling performance by measuring the thermal  
118 resistances, pressure drop and the resulting cooling coefficient-of-performance (COP), which  
119 indicates the energy efficiency of the heat sink. Fig. 3a shows the total thermal resistance ( $R_{tot}$ )  
120 between the surface temperature-rise and the inlet temperature for the evaluated structures.  
121 By reducing the SPMC channel dimensions from 100  $\mu\text{m}$  to 25  $\mu\text{m}$  at identical flow rates,  $R_{tot}$   
122 reduces, which can be attributed to the increased surface area for heat transfer. However, the  
123 4x- and 10x-mMMC heat sinks show an additional significant reduction in  $R_{tot}$  compared to the  
124 25  $\mu\text{m}$  SPMC, approaching the limit of single-phase water-cooling (defined by its heat  
125 capacity).  $R_{tot}$  was separated in three terms: the contribution due to the heating of the water  
126 based on its heat capacity ( $R_{cal}$ ), the contribution due to convective heat-transfer in the  
127 microchannels ( $R_{conv}$ ), and the contribution due to conduction ( $R_{cond}$ ). The full data reduction  
128 procedure to obtain these values is explained in the Methods section, as well as in Extended

129 Data Fig. 3. A breakdown of  $R_{tot}$  is shown in Fig. 3b, revealing a strong relation between  $R_{conv}$   
130 and microchannel size, where smaller channels reduce  $R_{conv}$ . A significant further decrease in  
131  $R_{conv}$  was achieved with the 10x-manifold, resulting in an 85% and 76% reduction compared  
132 to 50  $\mu\text{m}$  and 100  $\mu\text{m}$  SPMC, respectively. In combination with a very low  $R_{cond}$  for the co-  
133 designed manifolds, at a flow rate of 1.0 ml/s, a thermal resistance of 0.43 K/W was achieved.  
134 The 10x-manifold design thus allows heat fluxes up to 1723 W/cm<sup>2</sup> for a maximum temperature  
135 rise of 60 K, which is more than twice that of a 25 $\mu\text{m}$ -wide SPMC.

136 Narrow channels, however, require a higher pressure to achieve equal flow rate (Fig. 3c). For  
137 a flow rate of 0.5 ml/s, microchannel widths of 100  $\mu\text{m}$ , 50  $\mu\text{m}$  and 25  $\mu\text{m}$  require pressures of  
138 160 mbar, 260 mbar and 810 mbar, respectively. The manifold structure significantly lowers  
139 the pressure drop by reducing the length of the flow path through the microchannel. When  
140 splitting the flow in smaller sections with the 10x-manifold, the pressure drop reduced  
141 significantly to 210 mbar. This highlights the benefit of the MMC structure: a lower thermal  
142 resistance than SPMCs can be obtained at a reduced pumping power consumption. However,  
143 although the manifold structure can reduce the pressure drop, the additional contractions and  
144 turns of the fluid can hinder this reduction. For example, 20  $\mu\text{m}$ -wide microchannels in a 4x-  
145 manifold require a significantly higher pressure of 1300 mbar compared to 25  $\mu\text{m}$ -wide SPMC  
146 (Fig. 2d), which in part can also be attributed to the higher fluid velocity as the mMMC channels  
147 (125  $\mu\text{m}$ ) are not as deep as the SPMC (250  $\mu\text{m}$ ). These finding demonstrate the need for a  
148 carefully optimized geometry of the microchannel and manifold.

149 Fig. 3d shows a clear trend for SPMCs of increased effective base-area averaged heat-transfer  
150 coefficient ( $h_{eff}$ ) for smaller microchannels. This is due to the combined effect of the increased  
151 surface area and local heat-transfer coefficient in fully-developed laminar-flow regime. The co-  
152 designed mMMC structures with 4x-manifold channels and 20  $\mu\text{m}$ -wide microchannels  
153 matches this trend with  $h_{eff} = 3.1 \times 10^5 \text{ W/m}^2\text{-K}$ , but a large deviation from this pattern is  
154 observed when the effective length through which the coolant flows in the microchannel is  
155 reduced. For the 10x-manifold,  $h_{eff}$  more than doubles to  $7.3 \times 10^5 \text{ W/m}^2\text{K}$ , a rise that can be

156 accounted to the much-increased Nusselt number due to the developing flow in the MMC  
157 structure [27], [45]. This effect becomes more pronounced by considering the wall-area  
158 averaged heat-transfer coefficient ( $h_{wall}$ ) (Fig. 3e), which eliminates the contribution of the  
159 increased surface area from the heat-transfer coefficient, as well as accounts for the limited fin  
160 efficiency of the channels. Over a 3-fold increase in  $h_{wall}$  is observed between 25  $\mu\text{m}$ -straight  
161 microchannels and the 10-channel mMMC heat-sinks, up to  $2.4 \times 10^6 \text{ W/m}^2\text{-K}$ . This value  
162 corresponds to a remarkably high Nusselt number of 16, generally only achieved in larger-  
163 scale systems, or in more complex two-phase cooling systems, highlighting the superior  
164 thermal performance of this structure.

165 The combination of improved heat transfer and reduced pressure drop leads to significantly  
166 lower pumping power requirements. The cooling COP is defined as the ratio of extracted power  
167 to the pumping power required to provide such level of cooling, while maintaining a maximum  
168 surface temperature rise of 60K. Higher heat fluxes require higher flow rates, reducing the  
169 COP due to the larger pumping power required. Figure 3f benchmarks the evaluated devices,  
170 along with other technologies found in the literature. For SPMC, channel widths of 100  $\mu\text{m}$ , 50  
171  $\mu\text{m}$  and 25  $\mu\text{m}$  show a consecutively higher COP for higher heat fluxes, with a COP in the  
172 range between  $10^2$  and  $10^4$  and heat fluxes between  $350 \text{ W/cm}^2$  and  $800 \text{ W/cm}^2$ . The 10x-  
173 manifold device vastly outperforms these SPMCs. At an identical COP of  $5.0 \times 10^3$ , the 10x-  
174 manifold can sustain heat fluxes up to  $1.7 \text{ kW/cm}^2$  at 1.0 ml/s, compared to  $400 \text{ W/cm}^2$ ,  $450$   
175  $\text{W/cm}^2$  and  $550 \text{ W/cm}^2$  for 100  $\mu\text{m}$ , 50  $\mu\text{m}$  and 25  $\mu\text{m}$  SPMCs, respectively. Furthermore, at a  
176 heat flux of  $780 \text{ W/cm}^2$ , the 10x-manifold provides a 50-fold increase in COP with respect to  
177 25  $\mu\text{m}$  SPMCs. Compared to MMC heat sinks presented in the literature, the proposed mMMC  
178 device outperforms the current state-of-the-art, and demonstrates a significant potential for  
179 energy-efficient cooling by having a thermal-centered approach in the device design.

## 180 **Power IC with embedded cooling**

181 The lateral nature of AlGaIn/GaN electronics enables the monolithic integration of multiple  
182 power devices onto a single substrate. This opens a new horizon for power electronics, where

183 an entire converter can be integrated on a small chip, opening a large potential for energy,  
184 cost and space savings. However, the resulting high heat-fluxes limit the maximum output  
185 power of the chip. To demonstrate the potential of embedded cooling in a semiconductor  
186 device, we monolithically-integrated a full-bridge rectifier on a single GaN-on-Si die.  
187 Rectification was provided using four high-performance tri-anode Schottky barrier diodes  
188 (SBDs) with a breakdown voltage of 1.2 kV and high-frequency capability up to 5 MHz [46]. 50  
189  $\mu\text{m}$ -wide cooling channels were integrated on the silicon substrate (Fig. 4a). To fully benefit  
190 from the compactness of high-performance microchannel cooling, a novel 3-layer PCB with  
191 embedded coolant delivery channels was developed, used to guide the coolant to the device  
192 (Fig. 4b). The full fabrication of this monolithically-integrated power device and the PCB is  
193 described in the Methods, as well as shown in extended data Fig. 8. The device was finally  
194 fluidically connected to the PCB using laser-cut liquid- and solvent-resistant double-sided  
195 adhesive, providing a leak-tight connection. This method is low-cost and easy-to-prototype,  
196 but translates well to conventional solder bonding. Figures 4c,d show the converter  
197 implemented, with a very compact form factor, rectifying an AC signal with peak voltage/current  
198 of 150 V/1.2 A (Fig. 4e). Integrated liquid cooling led to a small temperature rise of 0.34 K per  
199 Watt of output power. For a maximum temperature rise of 60 K, this single die can thus produce  
200 an output power of 176 W at a flow rate of only 0.8 ml/s. Furthermore, the reduced operating  
201 temperature led to an increased conversion efficiency (Fig. 4f) by eliminating self-heating  
202 degradation from the electrical performance. The AC-DC converter was experimentally  
203 evaluated up to 120 W of output power, while the temperature rise stayed below 50 K (Fig.  
204 4g). Considering the small converter volume ( $4.8 \text{ cm}^3$ ), this corresponds to an ultra-high power-  
205 density of  $25 \text{ kW/dm}^3$ . Moreover, since all cooling occurs within its footprint, multiple devices  
206 can be densely packed on the same PCB to increase the output power. This is a clear benefit  
207 over conventional heat sinks relying on heat spreading to large areas. These results show that  
208 the proposed high-performance cooling approach can enable the realization of high-power  
209 (kW-range) converters of the size of USB-sticks in a foreseeable future.

## 210 **Discussion and outlook**

211 In this work, a new approach of co-designing microfluidics and electronics for energy-efficient  
212 cooling was presented, and demonstrated on GaN-on-Si power devices by turning the passive  
213 silicon substrate from a low-cost carrier into a high-performance heat sink. COP values above  
214  $10^4$  for heat fluxes surpassing  $1 \text{ kW/cm}^2$  could be obtained by focusing on cooling in an early  
215 stage of the device design. As a practical implication, the average added-energy expenditure  
216 of 34% for cooling in data centers could potentially drop below 0.01% by adopting this design  
217 approach. The entire mMMC cooling structure can be monolithically integrated in the substrate,  
218 requiring only conventional fabrication procedures, thus making this economically viable. To  
219 materialize this concept, new solutions in packaging and interconnects are required. The  
220 presented PCB-based fluid delivery provides an example of a strategy to use these co-  
221 designed chips, based on components familiar to the electronics designer. This consequently  
222 means that, in order to provide maximum energy savings, cooling should be an integral step  
223 in the entire electronic design chain, from the device to the PCB design, and not merely an  
224 afterthought. If these practicalities can be addressed, the co-design of microfluidic and  
225 electronics has the possibility to become a new paradigm in energy-efficient thermally-aware  
226 design of electronics. This may aid in solving critical challenges in electronics applications, as  
227 well as enabling future integrated power converters on a chip to support the electrification of  
228 our society in a sustainable manner.

## References

- [1] W. Haensch *et al.*, “Silicon CMOS devices beyond scaling,” *IBM J. Res. Dev.*, vol. 50, no. 4–5, pp. 339–361, 2006.
- [2] A. Kanduri, A. M. Rahmani, P. Liljeberg, A. Hemani, A. Jantsch, and H. Tenhunen, “A perspective on dark silicon,” in *The Dark Side of Silicon: Energy Efficient Computing in the Dark Silicon Era*, 2017, pp. 3–20.
- [3] N. Hardavellas, M. Ferdman, B. Falsafi, and A. Ailamaki, “Toward dark silicon in servers,” *IEEE Micro*, vol. 31, no. 4, pp. 6–15, Jul. 2011.
- [4] E. J. Nowak, “Maintaining the benefits of CMOS scaling when scaling bogs down,” *IBM Journal of Research and Development*, vol. 46, no. 2–3, pp. 169–180, 2002.
- [5] S. V. Garimella *et al.*, “Thermal challenges in next-generation electronic systems,” *IEEE Trans. Components Packag. Technol.*, vol. 31, no. 4, pp. 801–815, 2008.
- [6] H. OHASHI, “Recent Power Devices Trend,” *J. Inst. Electr. Eng. Japan*, vol. 122, no. 3, pp. 168–171, 2002.
- [7] IEA, “Together Secure Sustainable Digitalization & Energy,” 2017.
- [8] A. Shehabi *et al.*, “United States Data Center Energy Usage Report - LBNL-1005775,” 2016.
- [9] N. Jones, “How to stop data centres from gobbling up the world’s electricity,” *Nature*, vol. 561, no. 7722, pp. 163–166, 01-Sep-2018.
- [10] B. Agostini, M. Fabbri, J. E. Park, L. Wojtan, J. R. Thome, and B. Michel, “State of the Art of High Heat Flux Cooling Technologies,” *Heat Transf. Eng.*, vol. 28, no. 4, pp. 258–281, Apr. 2007.
- [11] R. C. Chu, R. E. Simons, M. J. Ellsworth, R. R. Schmidt, and V. Cozzolino, “Review of cooling technologies for computer products,” *IEEE Transactions on Device and Materials Reliability*, vol. 4, no. 4, pp. 568–585, Dec-2004.
- [12] U.S. Energy Information Administration. EIA, “2015 Residential Energy Consumption Survey (RECS),” 2015.
- [13] Water Research Foundation, “Residential End Uses of Water, Version 2,” 2016.
- [14] United States Census Bureau, “Annual Estimates of the Resident Population for

Incorporated Places of 50,000 or More, Ranked by July 1, 2018 Population: April 1, 2010 to July 1, 2018,” 2019.

- [15] EirGrid Group, “All-Island Generation Capacity Statement 2018-2027,” 2018.
- [16] H. Amano *et al.*, “The 2018 GaN power electronics roadmap,” *J. Phys. D. Appl. Phys.*, vol. 51, no. 16, p. 163001, Apr. 2018.
- [17] H. Ohashi, I. Omura, S. Matsumoto, Y. Sato, H. Tadano, and I. Ishii, “Power electronics innovation with next generation advanced power devices,” in *IEICE Transactions on Communications*, 2004, vol. E87-B, no. 12, pp. 3422–3429.
- [18] T. Wei *et al.*, “High-Efficiency Polymer-Based Direct Multi-Jet Impingement Cooling Solution for High-Power Devices,” *IEEE Trans. Power Electron.*, vol. 34, no. 7, pp. 6601–6612, Jul. 2019.
- [19] D. B. Tuckerman and R. F. W. Pease, “High-performance heat sinking for VLSI,” *IEEE Electron Device Lett.*, vol. 2, no. 5, pp. 126–129, May 1981.
- [20] D. Munding *et al.*, “Demonstration of high-performance silicon microchannel heat exchangers for laser diode array cooling,” *Appl. Phys. Lett.*, vol. 53, no. 12, pp. 1030–1032, Sep. 1988.
- [21] R. J. Phillips, “Microchannel Heat Sinks,” *Lincoln Lab. J. (ISSN 0896-4130)*, vol. 1, Spring 1988, p. 31-48., vol. 1, pp. 31–48, 1988.
- [22] G. M. Harpole and J. E. Eninger, “Micro-channel heat exchanger optimization,” in *1991 Proceedings, Seventh IEEE Semiconductor Thermal Measurement and Management Symposium*, 1991, pp. 59–63.
- [23] D. Copeland, M. Behnia, and W. Nakayama, “Manifold microchannel heat sinks: isothermal analysis,” *IEEE Trans. Components, Packag. Manuf. Technol. Part A*, vol. 20, no. 2, pp. 96–102, Jun. 1997.
- [24] D. Copeland, H. Takahira, W. Nakayama, and B. C. Pak, “Manifold microchannel heat sinks: Theory and experiment,” in *American Society of Mechanical Engineers, EEP*, 1995, vol. 10–2, no. January 1995, pp. 829–835.
- [25] D. Copeland, “Manifold microchannel heat sinks: numerical analysis,” in *American Society of Mechanical Engineers (Paper)*, 1995.
- [26] D. Copeland, M. Behnia, and W. Nakayama, “Manifold microchannel heat sinks: Conjugate and extended models,” *Int. J. Microelectron. Packag. Mater. Technol.*, vol. 1, no. 2, pp. 139–152, 1998.

- [27] R. Mandel, A. Shooshtari, and M. Ohadi, "A '2.5-D' modeling approach for single-phase flow and heat transfer in manifold microchannels," *Int. J. Heat Mass Transf.*, vol. 126, pp. 317–330, Nov. 2018.
- [28] E. Y. K. Ng and S. T. Poh, "Investigative study of manifold microchannel heat sinks for electronic cooling design," *J. Electron. Manuf.*, vol. 9, no. 2, pp. 155–166, Apr. 1999.
- [29] J. . H. Ryu, D. . H. Choi, and S. . J. Kim, "Three-dimensional numerical optimization of a manifold microchannel heat sink," *Int. J. Heat Mass Transf.*, vol. 46, no. 9, pp. 1553–1562, Apr. 2003.
- [30] S. Sarangi, K. K. Bodla, S. V. Garimella, and J. Y. Murthy, "Manifold microchannel heat sink design using optimization under uncertainty," *Int. J. Heat Mass Transf.*, vol. 69, pp. 92–105, 2014.
- [31] E. Cetegen, S. Dessiatoun, and M. Ohadi, "Heat transfer analysis of force fed evaporation on microgrooved surfaces," in *Proceedings of the 6th International Conference on Nanochannels, Microchannels, and Minichannels, ICNMM2008*, 2008, no. PART A, pp. 657–660.
- [32] E. Kermani, S. Dessiatoun, A. Shooshtari, and M. M. Ohadi, "Experimental investigation of heat transfer performance of a manifold microchannel heat sink for cooling of concentrated solar cells," in *Proceedings - Electronic Components and Technology Conference*, 2009, pp. 453–459.
- [33] K. P. Drummond *et al.*, "A hierarchical manifold microchannel heat sink array for high-heat-flux two-phase cooling of electronics," *Int. J. Heat Mass Transf.*, vol. 117, pp. 319–330, Feb. 2018.
- [34] D. Back *et al.*, "Design, Fabrication, and Characterization of a Compact Hierarchical Manifold Microchannel Heat Sink Array for Two-Phase Cooling," *IEEE Trans. Components, Packag. Manuf. Technol.*, vol. 9, no. 7, pp. 1291–1300, Jul. 2019.
- [35] W. Escher, T. Brunswiler, B. Michel, and D. Poulikakos, "Experimental Investigation of an Ultrathin Manifold Microchannel Heat Sink for Liquid-Cooled Chips," *J. Heat Transfer*, vol. 132, no. 8, p. 081402, Aug. 2010.
- [36] G. Schlottig, M. de Fazio, W. Escher, P. Granatieri, V. D. Khanna, and T. Brunswiler, "Lid-Integral Cold-Plate Topology: Integration, Performance, and Reliability," *J. Electron. Packag.*, vol. 138, no. 1, p. 010906, Mar. 2016.
- [37] A. J. Robinson, R. Kempers, J. Colenbrander, N. Bushnell, and R. Chen, "A single phase hybrid micro heat sink using impinging micro-jet arrays and microchannels,"

- Appl. Therm. Eng.*, vol. 136, pp. 408–418, May 2018.
- [38] L. Everhart, N. Jankowski, B. Geil, A. Bayba, D. Ibitayo, and P. McCluskey, “Manifold Microchannel Cooler for Direct Backside Liquid Cooling of SiC Power Devices,” in *ASME 5th International Conference on Nanochannels, Microchannels, and Minichannels*, 2007, pp. 285–292.
- [39] V. Gambin *et al.*, “Impingement cooled embedded diamond multiphysics co-design,” in *2016 15th IEEE Intersociety Conference on Thermal and Thermomechanical Phenomena in Electronic Systems (ITherm)*, 2016, pp. 1518–1529.
- [40] K. P. Drummond *et al.*, “Evaporative intrachip hotspot cooling with a hierarchical manifold microchannel heat sink array,” in *Proceedings of the 15th InterSociety Conference on Thermal and Thermomechanical Phenomena in Electronic Systems, ITherm 2016*, 2016, pp. 307–315.
- [41] C. Shekhar Sharma *et al.*, “Energy efficient hotspot-targeted embedded liquid cooling of electronics,” *Appl. Energy*, vol. 138, pp. 414–422, 2015.
- [42] V. K. Samalam, “Convective heat transfer in microchannels,” *J. Electron. Mater.*, vol. 18, no. 5, pp. 611–617, Sep. 1989.
- [43] A. Weisberg, H. H. Bau, and J. N. Zemel, “Analysis of microchannels for integrated cooling,” *Int. J. Heat Mass Transf.*, 1992.
- [44] J. H. Ryu, D. H. Choi, and S. J. Kim, “Numerical optimization of the thermal performance of a microchannel heat sink,” *Int. J. Heat Mass Transf.*, vol. 45, no. 13, pp. 2823–2827, Jun. 2002.
- [45] R. K. Shah and A. L. (Alexander L. London, *Laminar flow forced convection in ducts : a source book for compact heat exchanger analytical data*. Academic Press, 1978.
- [46] L. Nela, G. Kampitsis, J. Ma, and E. Matioli, “Fast-switching Tri-Anode Schottky Barrier Diodes for monolithically integrated GaN-on-Si power circuits,” *IEEE Electron Device Lett.*, pp. 1–1, 2019.

**Acknowledgements:**

We are grateful to the help of the staff at the Center of Micro and Nano Technology (CMI) for the support and advice on the fabrication processes. We would like to thank V. Navikas for his graphical assistance to the paper. This work was supported in part by the European Research Council (ERC Starting Grant) under the European Union's H2020 program/ERC Grant Agreement No. 679425, in part by the Swiss Office of Energy Grant No. SI501568-01 and in part by the Swiss National Science Foundation under Assistant Professor (AP) Energy Grant PYAPP2\_166901

**Author contributions:**

R.v.E. and E.M. conceived the project. R.v.E., R.S. and L.N. developed and optimized device fabrication processes. R.v.E. and L.N. fabricated the devices. R.v.E. designed and developed the experimental setup to study cooling performance. G.K. designed the circuits for evaluating the fabricated devices. R.v.E. and G.K. designed and performed the experiments. R.v.E. analysed the data. E.M. supervised the project. R.v.E. and E.M. wrote the manuscript with input from all authors.

**Competing interests:** The authors declare no competing interests.

## Figures

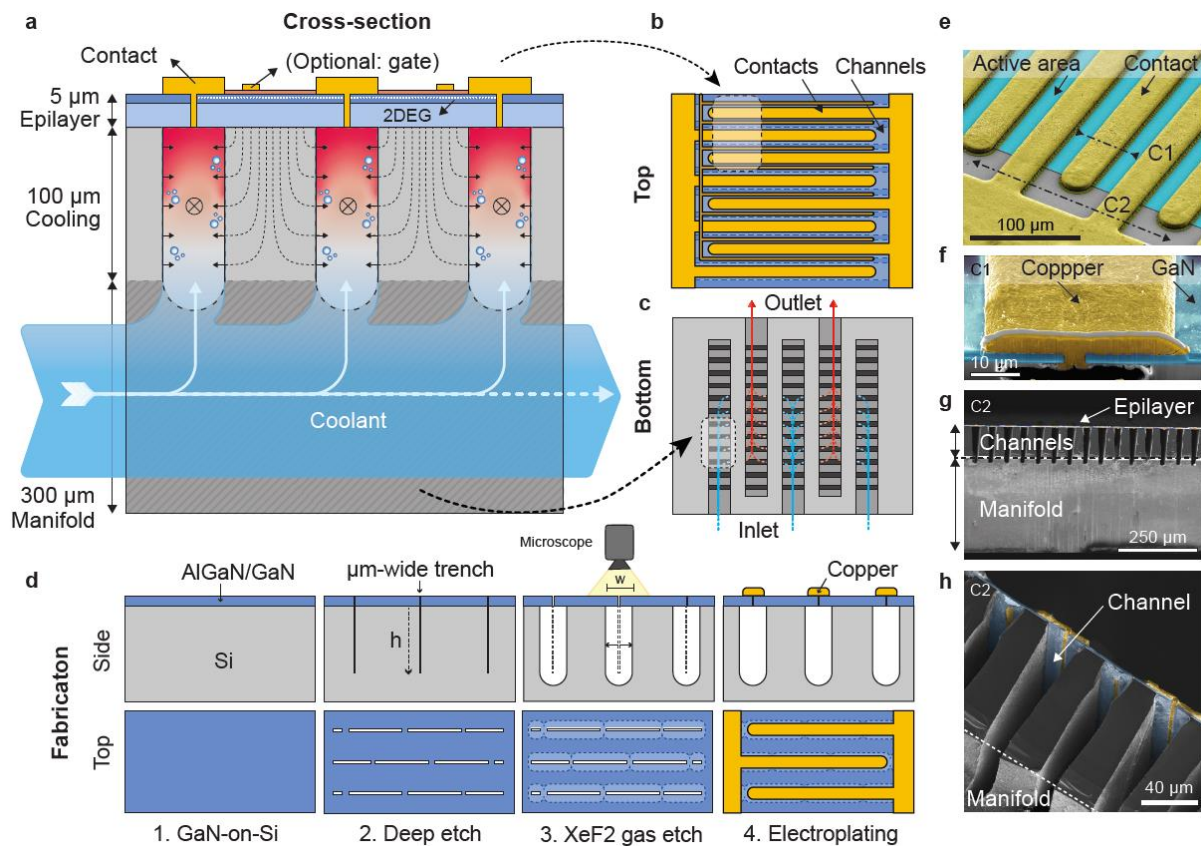


**Fig. 1 | Co-designed microfluidically-cooled electric device.** **a**, Schematic of the device structure, where the AlGaIn/GaN epilayer provides the electronic functions, and the silicon functions as cooling and fluid distribution manifold. Metal contacts seal the buried microchannels embedded underneath. Coolant coming from the manifolds flows in the out-of-plane orientation inside the microchannels to remove the heat away from the device. **b**, Top-view of the co-designed device structure: each contact is aligned and sealing the buried channel in a scaled-up multi-finger structure. **c**, Bottom-view, showing the manifold structure that distributes the flow over the microchannels. **d**, Summary of the proposed cooling method: A staggered pattern of narrow high aspect-ratio slits is first etched through the AlGaIn/GaN epilayer into the silicon. Next, an isotropic gas etch widens the channels in silicon, coalescing under the epilayer. The openings in the epilayer are then sealed using electroplating. **e**, Scanning electron microscopy (SEM) image of the AlGaIn/GaN surface after sealing the microchannels. Contact pads hermetically seal the incisions in the AlGaIn/GaN epilayer. **f**, Cross sectional SEM image along C1, showing the incision in the epilayer sealed with electroplated copper. **g**, Cross-sectional SEM image along C2, showing an array of buried microchannels, as well as a sidewall of the perpendicular manifold channel. **h**, Close-up of the cross section image along C2, showing the exposed microchannel below the electroplated-copper sealing-layer.

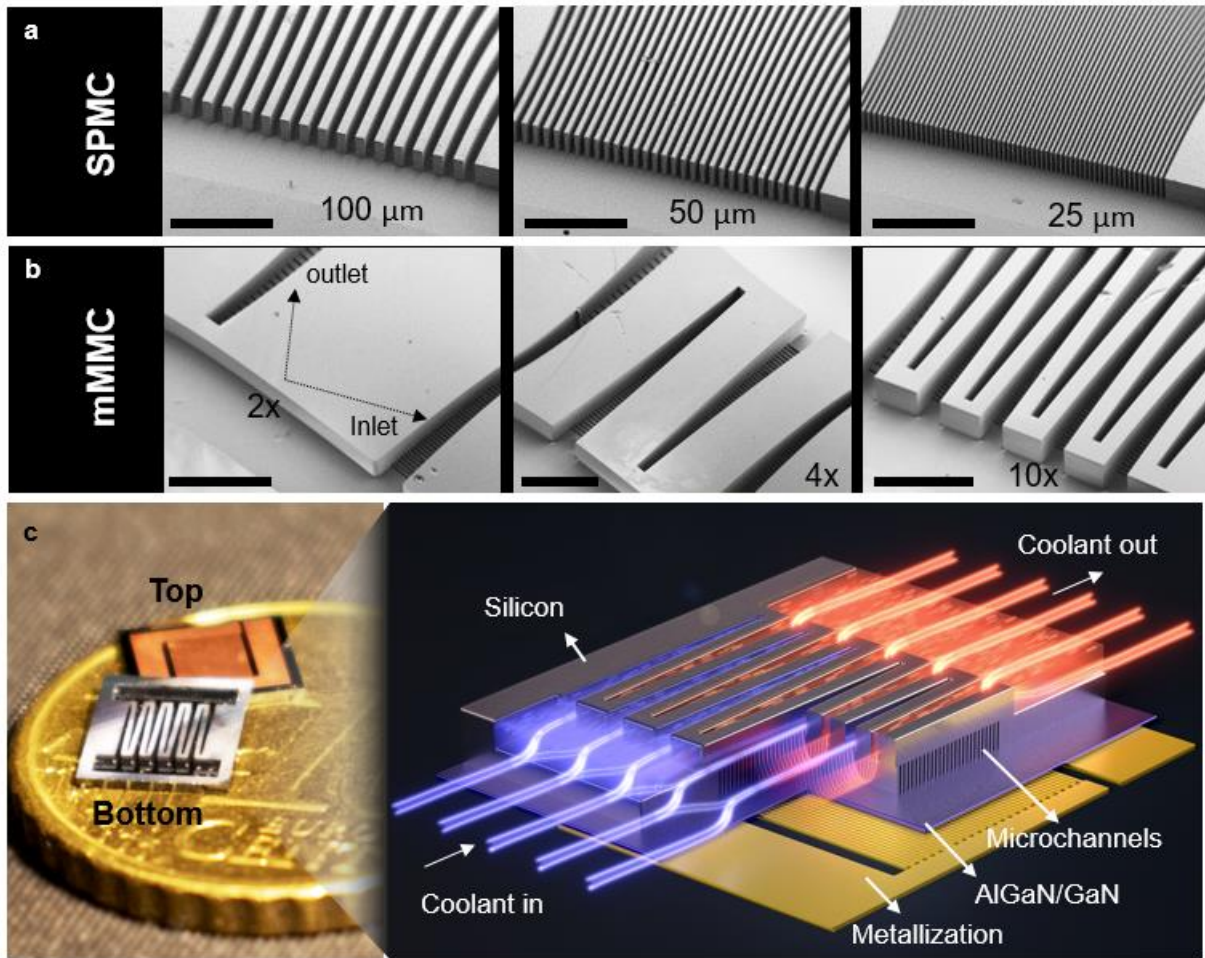


**Fig. 2 | Microchannel cooling configurations.** **a**, SEM images of the backside of the silicon substrate with SPMCs. Microchannel widths are 100  $\mu\text{m}$ , 50  $\mu\text{m}$  and 25  $\mu\text{m}$  and the scale bars represent 1 mm. **b**, SEM images of backside of the silicon substrate with mMMCs, with 2x, 4x and 10x-manifold sections. Scale bars represent 850  $\mu\text{m}$ . **c**, Picture of the co-designed devices, from the top and bottom sides, with 10x-manifold mMMC cooling. Top-side shows the electronic structure and the bottom shows the manifold etched in the silicon substrate. **d**, Illustration of the fluid flow through the mMMC structure. Blue lines indicate the cold coolant flow entering the chip, and red lines indicate the hot coolant leaving the chip.

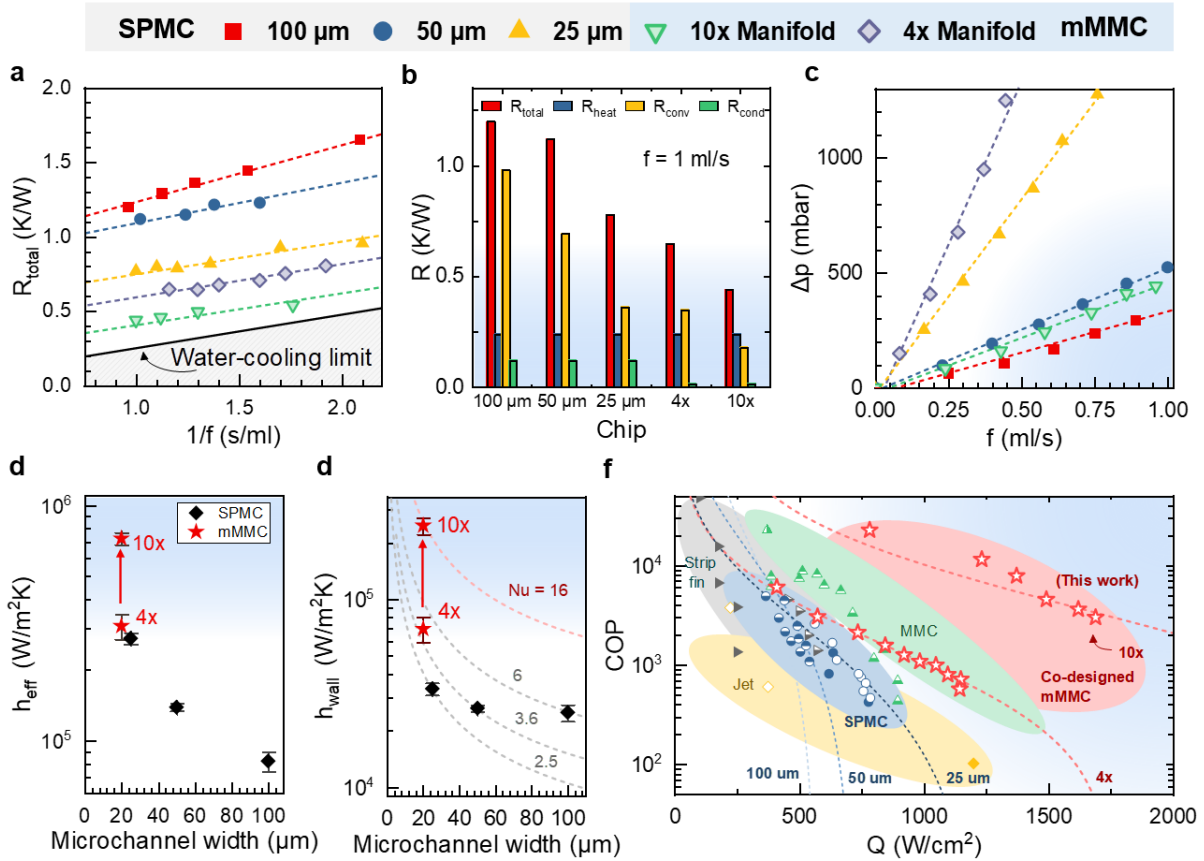


**Fig. 3. | Thermo-hydraulic evaluation of the cooling strategies.** **a**, Total thermal resistance between the surface temperature and the inlet temperature of the coolant. The black line indicates the lower limit of thermal resistance for single-phase water cooling, determined by its heat capacity. **b**, Breakdown of the contributions of  $R_{total}$ , into  $R_{heat}$ ,  $R_{conv}$  and  $R_{cond}$ , for all evaluated devices. **c**, Pressure drop versus flow rate for the considered microchannel structures. The 4x- and 10x-manifold had 20  $\mu\text{m}$ -wide channels. **d**, Effective (base-area averaged) heat-transfer coefficient for straight (SPMC) and manifold (mMMC) structures. **e**, Wall-averaged heat-transfer coefficient for straight and manifold microchannels. A 4.4-time increase in Nusselt number was observed between the 4x- and 10x-manifold. **f**, Benchmark of the experimentally-demonstrated coefficient of performance (COP) versus the maximum heat flux for a temperature rise of 60 K. SPMC (blue) MMC (Green), Impinging jet (Yellow), strip-fin (grey) and mMMC (red) and are shown. More extensive benchmarking with simulation/analytical results, full references and further classification is provided in Extended Data Fig. 6. And Extended Data Table 2. A significant improvement in COP for a given heat flux is achieved with our proposed mMMC structures (red). Dashed lines are models for COP vs heat flux, under the assumption of a constant heat transfer coefficient and a linear pressure-flowrate relation, fitted through the experimental data.

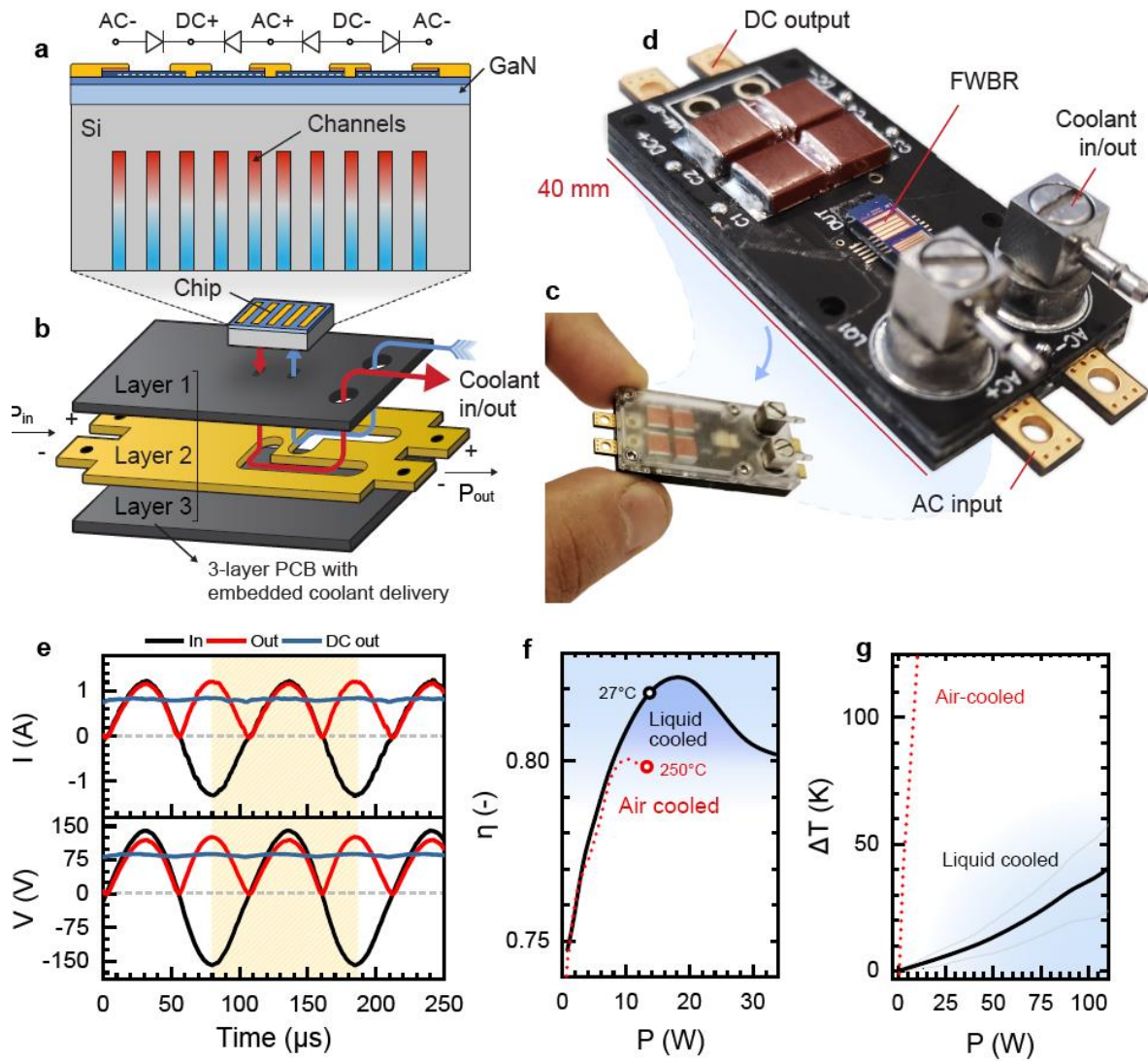


**Fig. 4. | AC-DC Converter with embedded liquid cooled GaN power IC.** **a**, Schematic illustration of the super-compact liquid-cooled power IC based on four GaN power SBDs integrated in a single chip in a full-bridge configuration. **b**, A PCB-embedded coolant delivery was developed to feed the coolant to the device. The PCB consists of 3 layers, where the middle layer contains a fluid distribution channel. **c**, Picture of the full 120 W AC-DC converter with coolant delivery to the liquid-cooled power IC. **d**, Converter without encapsulation, revealing the monolithically-integrated Full-Wave Bridge-Rectifier (FWBR) IC. **e**, Converter 150 V AC input (black) and output before (red) and after (blue) filtering using output capacitors. **f**, Efficiency versus output power for the air-cooled and liquid-cooled AC-DC converter. At identical output power, the liquid cooled converter exhibits significantly higher efficiency due to elimination of self-heating degradation. **g**, Temperature rise versus output power, showing a significantly higher temperature at equal output power for the air-cooled device compared to the embedded liquid cooling, which causes a large self-heating degradation.

## 1 METHODS

2 **Device fabrication process.** The fabrication process of the co-designed microfluidic-  
3 electronic device is shown in Extended Data Fig 1. Fabrication started with an AlGaIn/GaN-on-  
4 silicon wafer with, from top to bottom: 2.9 nm GaN cap-layer, 20 nm AlGaIn barrier, 420 nm  
5 GaN channel, 4.2  $\mu\text{m}$  buffer layer, on a 400  $\mu\text{m}$ -thick silicon. First, a mesa was etched to define  
6 the active area of the chip, followed by a 1  $\mu\text{m}$ -thick plasma-enhanced chemical vapor  
7 deposition (PECVD) of  $\text{SiO}_2$  as an etching mask to obtain sharp sidewalls after GaN etching.  
8 Photoresist was lithographically patterned on top of the  $\text{SiO}_2$  layer, to define and open a  
9 staggered pattern of slits in the  $\text{SiO}_2$  mask using inductively coupled plasma (ICP) etching  
10 using  $\text{C}_4\text{F}_8$  chemistry. The staggered pattern, with 30  $\mu\text{m}$ -long slits spaced 2  $\mu\text{m}$  apart,  
11 prevented the epilayer from turning into a fragile cantilever after performing an undercut in the  
12 silicon substrate. Instead, the 2  $\mu\text{m}$  spacing between each slit kept the epilayer together,  
13 resulting in good mechanical integrity of the epilayer during the fabrication process. The  
14 photoresist was stripped using an  $\text{O}_2$  plasma and the exposed GaN slits were consecutively  
15 etched using  $\text{Cl}_2+\text{Ar}$  chemistry until the silicon substrate was reached, which was confirmed  
16 using end-point detection. The chips were then dipped into 40% KOH at 60°C for 5 minutes to  
17 remove any remaining AlN-based material from the buffer [47], [48]. The Bosch process was  
18 used to etch the silicon slits for approximately 115  $\mu\text{m}$  deep, resulting in high aspect ratio slits.  
19 The microchannels in silicon were widened using an isotropic  $\text{XeF}_2$  gas etch, which provided  
20 selectivity over GaN [49].  $\text{XeF}_2$  gas etching was performed in a pulsed manner: The sample  
21 was exposed to  $\text{XeF}_2$  at a controlled pressure (1.33 mbar) for 30 seconds, followed by  
22 evacuation of the etching chamber. This process was repeated for 45 cycles until the desired  
23 channel width was obtained. In-situ optical etching tracking through the transparent GaN  
24 membrane was performed using a camera directly mounted on the etching chamber, as shown  
25 in Extended Data Fig. 1. This method enabled to accurately obtain the desired channel width,  
26 and to ensure that all slits were coalesced into continuous channels underneath the epilayer.  
27 This way, 20- $\mu\text{m}$  wide microchannels were etched through the narrow openings in the epilayer.  
28 Next, the  $\text{SiO}_2$  hard mask was stripped using 50% HF for 10 minutes, and the surface was

29 further cleaned from all organic residues using piranha treatment. A Ti/Al/Ti/Ni/Au Ohmic  
30 contact stack was deposited using e-beam evaporation and photolithographically patterned by  
31 lift-off, followed by an annealing step at 850 °C. The in- and outlet channels were etched in the  
32 backside of the chip using the Bosch process, until the channels from both sides coalesced,  
33 which was confirmed by optical microscopy. The slits in the GaN epilayer were then sealed by  
34 electroplating approximately 7  $\mu\text{m}$  of copper on top of the Ohmic contacts. For the  
35 electroplating process, a uniform seed layer of chromium-copper (20nm/70nm) was deposited  
36 on top of the device after the contact metallization step using e-beam evaporation, where  
37 chromium served as an adhesion layer and copper as the seed layer. Next, 10  $\mu\text{m}$  of  
38 photoresist was patterned to define the area to be electroplated. Electrical contact was made  
39 to the chip, which functions as cathode, using electrically conductive adhesive that was applied  
40 over all edges of the chip. First, the chip was shortly dipped in  $\text{H}_2\text{SO}_4$  to remove any surface  
41 oxidation. Then, electroplating was performed using a galvanostat at 1 A for 7 min minutes in  
42 a solution containing  $\text{CuSO}_4$ ,  $\text{H}_2\text{SO}_4$  and  $\text{Cl}^-$ , as well as an addition of Intervia 8510 (Dow),  
43 while using a CuP anode. As the galvanically deposited copper film grows conformally and  
44 isotropically, the incisions in the GaN layer seal as the copper layer bridges the gap and  
45 coalesces on top of the cavity. After electroplating, the photoresist was stripped, and the seed  
46 layer was etched by performing a short copper wet-etch ( $(\text{NH}_4)_2\text{S}_2\text{O}_8 + \text{H}_2\text{SO}_4$ ), followed by a  
47 chromium etch that is selective over copper ( $\text{KMnO}_4 + \text{Na}_3\text{PO}_4$ ). Finally, the individual dies  
48 were separated using a dicing saw. The video in the Supplementary Information illustrates the  
49 flow-path of the coolant through this mMMC heat sink structure.

50 **Experimental setup for evaluation of cooling performance.** An open loop single-phase  
51 liquid cooling setup, schematically shown in Extended Data Figure 2a was built underneath an  
52 IR camera in order to perform liquid cooling experiments, as can be seen in Extended Data  
53 Figure 2b. A reservoir of deionized (DI) water was pressurized with compressed air using a  
54 pressure controller (Elveflow OB1 MK2), causing it to flow towards the test section manifold  
55 machined out of polyetheretherketone (PEEK) (Extended Data Figure 2c). PEEK was chosen

56 because of its low thermal conductivity, preventing heat flux to leak out of the system by  
57 conduction, as well as because of its high glass-transition temperature of 143 °C [50]. The flow  
58 rate of the coolant was measured using a thermal mass flow sensor (Sensirion SLQ-QT500).  
59 Chips are mounted on laser-cut Poly(methyl methacrylate) (PMMA) carriers with double-sided  
60 adhesive and connected to the test section using laser-cut silicone gaskets. A closed seal was  
61 obtained on these gaskets using 4 screws that push down on the PMMA carriers. This way,  
62 no force needs to be applied directly on the chips, preventing the chips from breaking during  
63 mounting. Two pressure sensors (Elveflow MPS) were used to measure the pressure at the  
64 inlet and outlet of the chip, and the inlet and outlet fluid temperatures are measured using a  
65 type-K thermocouple (THERMOCAOX), integrated right before the inlet and right after the  
66 outlet of the chip. The thermocouples were calibrated using a thermostatic bath (Lauda  
67 RP855). The chips were connected to a power supply (TTI QPX1200), which simultaneously  
68 applies a voltage and measures the current over the device under test (DUT). Electrical  
69 connection with the DUT was made using 6 high-current-rated spring-loaded pins, connected  
70 to a custom-made PCB with a hole in the center to allow infrared (IR) measurements.  
71 Temperature rise on the surface of the chip was measured using a FLIR SRC3000 IR camera.  
72 A LabVIEW automation program was developed to automate the data acquisition. The  
73 program waits for the liquid outlet temperature to stabilize, then sends a trigger signal to the  
74 video card of the PC connected to the IR camera to record 20 snapshots, and increases the  
75 power dissipated on the chip until a critical surface temperature was reached. The surface of  
76 the chip was painted black using spray paint to increase emissivity. To further improve the  
77 accuracy of the IR thermography, a pixel-by-pixel emissivity calibration was performed by  
78 flowing water at a controlled temperature using the thermostatic bath following the method  
79 described in [51]. IR emission was measured at each temperature and a fit between  
80 temperature and IR emission was established for each pixel of the photodetector. Finally, a  
81 MATLAB script was developed in order to automate the post-processing of the IR data, which  
82 gave the mean surface temperature rise and the maximum surface temperature rise. The latter

83 was defined as the mean value of the 20 highest temperature readings, to be less susceptible  
84 to noise.

85 **Pressure test.** Before evaluating the cooling performance, pressure tests were performed by  
86 increasing the system pressure of up to 4 bar (above atmospheric) on each chip. This  
87 procedure was intended as a burst test, but no failure was observed up to the maximum  
88 pressure capability of the experimental facility. It should be noted that typical epitaxial growth  
89 of AlGaIn/GaN on a silicon substrate using metal-organic chemical vapor deposition is  
90 performed at temperatures around 1000 °C. Due to the mismatch in coefficient of thermal  
91 expansion, the resulting stress in the epilayer is in typically in the order of 0.3 GPa, whereas  
92 the critical cracking stress lies around 1.1 GPa [52]. Although the additional pressure inside  
93 the channels during liquid flow does contribute to the total stress in the epilayer, 1 bar (typical  
94 operation) equals to only 0.1 MPa. This stress is more than three orders of magnitude smaller  
95 than the typical residual stress in the epilayer, and is therefore not expected to cause failure.  
96 This finding agrees with our observations, as well as with other works in the literature [53], [54].

97 **Data reduction.** The cooling performance of all chips was analyzed for power dissipations up  
98 to 75 W and flow rates between 0.1-1.1 ml/s. Extended Data Fig. 3 shows an overview of the  
99 data reduction procedure for the 10x-manifold chip to obtain the relevant values in Fig. 3. The  
100 maximum surface temperature ( $\Delta T_{surface}$ ) rise was calculated by subtracting the coolant inlet  
101 temperature from the maximum IR-measured surface temperature (Extended Data Fig. 3a).  
102 The liquid temperature rise ( $\Delta T_{liquid}$ ) was calculated by subtracting the inlet water temperature  
103 from the water outlet temperature, measured by thermocouple (Extended Data Fig. 3b). The  
104 wall temperature ( $\Delta T_{wall}$ ) was calculated by subtracting the mean water temperature between  
105 the inlet and outlet from the average surface temperature rise, and performing a correction for  
106 1D conduction through the epilayer, thermal boundary resistance and silicon in case of the  
107 straight channels (Extended Data Fig. 3c). A thermal boundary resistance between the GaN  
108 and silicon substrate of  $1.0 \times 10^{-7} \text{ W}^{-1} \cdot \text{m}^2 \cdot \text{K}$  was assumed [55]–[57]. The effective applied  
109 power was calculated using an energy balance ( $P = \rho \cdot c_p \cdot \Delta T_{liquid}$ ), where  $\rho$  and  $c_p$  are the density

110 and heat capacity of water, respectively. For all flow-rates, the total thermal resistance ( $R_{tot}$ ),  
 111 the caloric thermal resistance ( $R_{cal}$ ) and convective thermal resistance ( $R_{conv}$ ) were determined  
 112 through a linear fit of the surface temperature rise (Fig. 3a), coolant temperature rise (Extended  
 113 Data Fig. 4b) and wall temperature rise (Extended data fig. 4a) versus dissipated power,  
 114 respectively. Thus, every point in Extended Data Fig. 3d was derived from a wide range of  
 115 measurements to ensure a high accuracy. This figure was plotted against the inverse flow rate  
 116 to highlight the linear relationship between  $R_{cal}$  and  $f^{-1}$ . As can be seen, most of the variation  
 117 of  $R_{tot}$  with flow-rate can be accounted to  $R_{cal}$ , whereas  $R_{conv}$  shows little dependence on the  
 118 flow-rate. COP was calculated by dividing the maximum heat flux for a  $\Delta T_{max}$  of 60 degrees  
 119 temperature rise by the required pumping power ( $P_{pump}$ ) to achieve this level of cooling [58]  
 120 ( $COP = \Delta T_{max} / P_{pump} \cdot R_{tot}$ ), where pumping power was calculated as the product of flow rate and  
 121 pumping power ( $P_{pump} = f \cdot \Delta p$ ). Effective base-area averaged heat transfer coefficient was  
 122 calculated using  $h = (R_{conv} \cdot A_{device})^{-1}$ , where  $A_{die}$  represents the footprint area of the active area  
 123 of the device, containing both the electric device and the cooling structure. Average local heat  
 124 transfer coefficient ( $h_{wall}$ ) was determined by taking the fin efficiency ( $\eta$ ) into account, which  
 125 was calculated using  $\eta = 1$  as a starting point for iteratively solving [59], [60]

$$126 \quad \eta = \frac{\tanh\left(z \sqrt{\frac{2h_{wall}}{k_{si}w_w}}\right)}{z \sqrt{\frac{2h_{wall}}{k_{si}w_w}}}$$

127 Here,  $z$  represents the channel depth,  $w_w$  the channel wall width and  $k_{si}$  is the thermal  
 128 conductivity of the silicon substrate, which was chosen to be 150 W/m-K. Finally, based on  
 129  $h_{wall}$ , the average Nusselt number (Nu) was calculated for each measurement condition using  
 130  $Nu = h_{wall} \cdot D_h / k_{water}$ , where  $D_h$  is the hydraulic diameter of the channel ( $D_h = (2 \cdot w_c \cdot z) / (w_c + z)$ ) and  
 131  $k_{water}$  the thermal conductivity of water at the mean measured temperature. Extended Data Fig.  
 132 5 shows a complete overview of the remaining datasets for temperature rise and thermal  
 133 resistance of the 25  $\mu m$ /50  $\mu m$ /100  $\mu m$ -SPMC and 4x-mMMC, and the full overview of the  
 134 design parameters and derived values is presented in Extended Data Table 1. Extended data

135 Fig. 3e shows the Nusselt number and fin efficiency over the measured range of flow speeds,  
136 and Extended Data Fig. 3f shows both the effective base-area averaged and average local  
137 heat transfer coefficients. In thermally-developing laminar internal flow, the observed average  
138 Nusselt number is expected to increase with flow rate, due to the increased entrance length.  
139 At higher flow rates, a longer entrance length will result in a higher heat transfer coefficient.  
140 This general trend is observed in Extended Data Fig. 4(d). For the 10x manifold, this effect  
141 saturates, likely due to the short length of the channels, which in combination with a potential  
142 shift in coolant distribution over the chip at higher Reynolds number, causes the Nusselt  
143 number to peak. A complete overview of the fin efficiencies and Nusselt numbers for all devices  
144 can be found in Extended Data Fig. 4c-d. Extended Data Fig. 5 shows the additional thermo-  
145 hydraulic analysis on all evaluated devices used for deriving their cooling performance.  
146 Extended Data Table 1 summarizes all dimensions and cooling performance of the chips. The  
147 performance of the mMMC chips, as well as the SMPC chips evaluated in this work were  
148 benchmarked against a wide range of works in the literature that use water as a coolant  
149 (Extended Data Fig. 6). The cooling approaches were classified as SPMC ([19], [61]), Pin-fins  
150 ([61], [62]), Strip-fins ([61], [63], [64]), MMC ([29], [65]–[68][69]), Impinging jet ([37], [61], [70]–  
151 [72]), and mMMC (This work). A distinction was made between: techniques where the water is  
152 in direct contact with the die and the die contains cooling structures (embedded cooling),  
153 approaches where the water is in direct with the die, but the die itself does not contain cooling  
154 structures (bare-die cooling), and indirect cooling, which requires an additional thermal  
155 interface between the heat sink and the chip. A tabulated file with all data points used in the  
156 benchmarking study can be found in the supplementary data.

157 **Impact of hydrostatic pressure on electrical performance.** Due to the piezoelectric  
158 properties of GaN, changes in pressure and the resulting strain in the epilayer may affect the  
159 electrical performance of the device [53], [73]. In order to investigate this phenomena, the  
160 outlet of the test section in Extended Data Fig. 2 was plugged. The hydrostatic pressure applied  
161 to the test section was swept from 0 mbar to 1590 mbar and back. At each step in pressure, a

162 cyclic IV-measurement was performed, together with the measurement of the water  
163 temperature in the test section. After the water reached ambient temperature, the next  
164 measurement was performed. This was done to prevent any drift in temperature during the 3-  
165 hour-long measurement, which might affect the resistance of the chip. The 14 IV-  
166 characteristics (Extended Data Fig. 7a) show no clear impact on device performance. Next,  
167 the on-resistance was derived from the IV curves using a linear fit at each pressure condition.  
168 The observed variation in on-resistance remained within 1.5% of its initial value at atmospheric  
169 pressure (Extended Data Fig. 7b). These results show that the effect of the pressure range  
170 considered here on the electrical properties of the devices is negligible for the purpose of this  
171 work. The reason for the small impact of this effect on electrical performance could be  
172 accounted to the fact that the microchannels are positioned below the pads, and covered with  
173 metal. Any change in carrier density in this region of the chip due to strain would not  
174 significantly affect the device performance, as most contribution to the device's resistance is  
175 in the area between the pads.

176 **AC-DC converter fabrication.** Tri-anode SBD full-wave bridge rectifiers (FWBR) were  
177 fabricated on an AlGaIn/GaN-on-silicon wafer with, from top to bottom: a 2.9nm GaN cap layer,  
178 20 nm AlGaIn barrier, 420 nm GaN channel and a 4.2  $\mu\text{m}$  buffer layer on a 400  $\mu\text{m}$ -thick silicon  
179 substrate. Tri-anode/tri-gate regions were first defined using e-beam lithography with a width  
180 and spacing of 200 nm, followed by a 200 nm-deep inductively coupled plasma etch following  
181 the process previously described in [46]. These dimensions have been shown to result in high  
182 breakdown voltage and excellent on-state performance [74]. After Ohmic metal deposition for  
183 the cathode contacts, 20 nm-thick  $\text{SiO}_2$  was deposited by atomic layer deposition as the tri-  
184 gate dielectric, and then selectively removed in the tri-anode region. A Ni/Au metal stack was  
185 deposited on the tri-gate/tri-anode region to form the Schottky contact, as well as on the  
186 cathode. Extended Data Fig. 8d shows a SEM image of four scaled-up tri-gate SBDs forming  
187 the FWBR. The close-up SEM image shows the SBD structure. The channel length was 16.5  
188  $\mu\text{m}$ , corresponding to 1.2 kV of breakdown voltage [46]. Next, the wafer was temporarily

189 bonded to a carrier wafer before microchannels were etched in the backside using deep  
190 reactive ion etching to a depth of approximately 500  $\mu\text{m}$ . After detaching the substrate from  
191 the carrier wafer and dicing, the individual liquid-cooled FWBR was attached to a 3-layer PCB  
192 using water-resistant adhesive with embedded coolant delivery channels. The top-layer PCB  
193 provides the electric circuit connections and the middle layer contains the coolant delivery  
194 channels (Extended Data Fig. 8a). The individual layers of the PCB were connected in an easy  
195 manner using laser cut adhesive (Extended Data Fig. 8b). Medical-grade pressure-sensitive  
196 double-sided adhesive was used from AR-Global (ARseal 90880), with water- and solvent-  
197 resistant properties as well as high temperature operation range (up to 120  $^{\circ}\text{C}$ ). A rectangular  
198 piece with inlet and outlet holes was laser-cut using a  $\text{CO}_2$  laser. The double-sided adhesive  
199 was placed on the PCB, aligning the inlet and outlet holes of the adhesive with the PCB. Next,  
200 the chip was attached to adhesive on the PCB to create a seal. This approach emphasizes the  
201 possibility to assemble a prototype without the need of expensive machines. Alternatively,  
202 since the PCB contains a gold-plated metalized landing pad, conventional large-scale  
203 industrial processes can be utilized as well, such as (eutectic) solder bonding between a  
204 metallization layer on the backside of the chip and the PCB. Extended Data Fig. 8c shows the  
205 final assembled converter.

206 **AC-DC converter evaluation.** The cooling performance of the AC-DC converter was  
207 investigated by connecting all four SBDs in parallel, such that a uniform known DC power  
208 dissipation could be applied to the chip. For flow rates varying between 0.08 and 0.8 ml/s, the  
209 surface temperature rise was monitored increasing power dissipation up to 25 W (Extended  
210 Data Fig. 9b). The flow-rate dependent thermal resistance was derived from the slopes of  
211 surface-temperature versus power (Extended Data Fig. 9c). For each flow rate, pressure drop  
212 between the inlet and outlet was measured, and the corresponding pumping power was  
213 calculated (Extended Data Fig. 9d). Over the entire range of measured flow rates, the total  
214 pumping power stayed below 62 mW, which can be easily supplied by miniaturized  
215 piezoelectric micropumps to achieve a high system-level power density. To study the power-

216 conversion performance of the AC-DC converter, the device was connected to a full-bridge  
217 inverter with LC filter to supply a 100 kHz AC input, up to 200 V peak to peak. The DC output  
218 of the converter was connected to a load of 50  $\Omega$ , and flow-rate was fixed at 0.8 ml/s. Extended  
219 Data Fig. 9a shows the input AC and output DC waveforms of the converter at 70 W of  
220 transferred power. Surface temperature was monitored using an IR camera, while power was  
221 increased until a critical surface temperature rise of 60 K was observed. Following this  
222 approach, up to 120 W of output power could be delivered using this compact power converter.

## Methods references

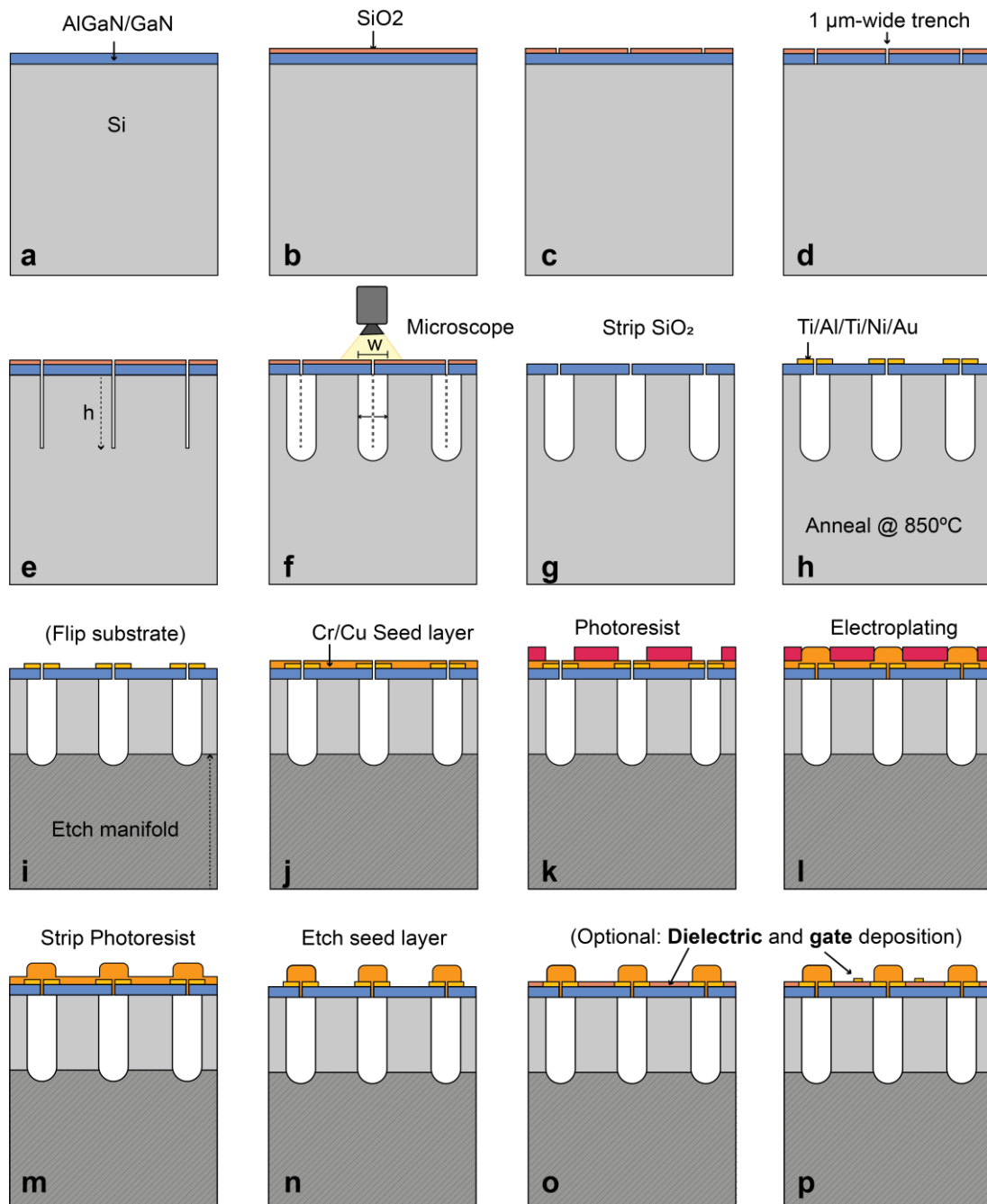
- [47] J. R. Mileham, S. J. Pearton, C. R. Abernathy, J. D. Mackenzie, R. J. Shul, and S. P. Kilcoyne, "Wet chemical etching of AlN," *Cit. Appl. Phys. Lett.*, vol. 67, no. 1119, 1995.
- [48] W. Guo *et al.*, "KOH based selective wet chemical etching of AlN, Al<sub>x</sub>Ga<sub>1-x</sub>N, and GaN crystals: A way towards substrate removal in deep ultraviolet-light emitting diode," *Appl. Phys. Lett.*, vol. 106, no. 8, p. 82110, 2015.
- [49] S. Vicknesh, S. Tripathy, V. K. X. Lin, L. S. Wang, and S. J. Chua, "Fabrication of deeply undercut GaN-based microdisk structures on silicon platforms," *Appl. Phys. Lett.*, vol. 90, no. 7, p. 71906, 2007.
- [50] A.K. van der Vegt & L.E. Govaert, *van keten tot kunstof*. DUP Blue Print, 2003.
- [51] S. Szczukiewicz, N. Borhani, and J. R. Thome, "Fine-resolution two-phase flow heat transfer coefficient measurements of refrigerants in multi-microchannel evaporators," *Int. J. Heat Mass Transf.*, vol. 67, pp. 913–929, 2013.
- [52] S. Raghavan and J. M. Redwing, "Growth stresses and cracking in GaN films on (111) Si grown by metal-organic chemical-vapor deposition. I. AlN buffer layers," *J. Appl. Phys.*, vol. 98, no. 2, p. 023514, Jul. 2005.
- [53] C. A. Chapin, R. A. Miller, K. M. Dowling, R. Chen, and D. G. Senesky, "InAlN/GaN high electron mobility micro-pressure sensors for high-temperature environments," *Sensors Actuators, A Phys.*, vol. 263, pp. 216–223, Aug. 2017.
- [54] X. Tan *et al.*, "High performance AlGaIn/GaN pressure sensor with a Wheatstone bridge circuit," *Microelectron. Eng.*, vol. 219, p. 111143, Jan. 2020.
- [55] A. Sarua *et al.*, "Thermal boundary resistance between GaN and substrate in AlGaIn/GaN electronic devices," *IEEE Trans. Electron Devices*, vol. 54, no. 12, pp. 3152–3158, Dec. 2007.
- [56] V. O. Turin and A. A. Balandin, "Performance degradation of GaN field-effect transistors due to thermal boundary resistance at GaN/substrate interface," *Electron. Lett.*, vol. 40, no. 1, pp. 81–83, Jan. 2004.
- [57] J. Kuzmík *et al.*, "Transient thermal characterization of AlGaIn/GaN HEMTs grown on silicon," *IEEE Trans. Electron Devices*, vol. 52, no. 8, pp. 1698–1705, Aug. 2005.
- [58] M. E. Steinke and S. G. Kandlikar, "SINGLE-PHASE LIQUID HEAT TRANSFER IN PLAIN AND ENHANCED MICROCHANNELS," 2006.

- [59] I. Tosun, *Modeling in Transport Phenomena*. Elsevier, 2007.
- [60] J. E. Hesselgreaves, R. Law, and D. A. Reay, "Chapter 7 - Thermal Design," *Compact Heat Exch. (Second Ed., vol. I, pp. 275–360, 2017.*
- [61] S. Ndao, Y. Peles, and M. K. Jensen, "Multi-objective thermal design optimization and comparative analysis of electronics cooling technologies," *Int. J. Heat Mass Transf.*, vol. 52, no. 19–20, pp. 4317–4326, Sep. 2009.
- [62] T. Brunswiler *et al.*, "Interlayer cooling potential in vertically integrated packages," in *Microsystem Technologies*, 2009, vol. 15, no. 1 SPEC. ISS., pp. 57–74.
- [63] S. G. Kandlikar and H. R. Upadhye, "Extending the heat flux limit with enhanced microchannels in direct single phase cooling of computer chips," *Semicond. Therm. Meas. Manag. IEEE Twenty First Annu. IEEE Symp. 2005.*, pp. 8–15, 2005.
- [64] E. G. Colgan *et al.*, "A practical implementation of silicon microchannel coolers for high power chips," in *Annual IEEE Semiconductor Thermal Measurement and Management Symposium*, 2005, pp. 1–7.
- [65] K. W. Jung *et al.*, "Embedded cooling with 3D manifold for vehicle power electronics application: Single-phase thermal-fluid performance," *Int. J. Heat Mass Transf.*, vol. 130, pp. 1108–1119, Mar. 2019.
- [66] W. Escher, T. Brunswiler, B. Michel, and D. Poulikakos, "Experimental Investigation of an Ultrathin Manifold Microchannel Heat Sink for Liquid-Cooled Chips," *J. Heat Transfer*, vol. 132, no. 8, p. 081402, Aug. 2010.
- [67] M. Ohadi, K. Choo, S. Dessiatoun, and E. Cetegen, "Next Generation Microchannel Heat Exchangers," in *SpringerBriefs in Applied Sciences and Technology*, no. 9781461407782, New York, NY: Springer New York, 2013, pp. 1–111.
- [68] Y. Han, B. L. Lau, G. Tang, X. Zhang, and D. M. W. Rhee, "Si-Based Hybrid Microcooler with Multiple Drainage Microtrenches for High Heat Flux Cooling," *IEEE Trans. Components, Packag. Manuf. Technol.*, vol. 7, no. 1, pp. 50–57, Jan. 2017.
- [69] Y. Han, B. L. Lau, X. Zhang, Y. C. Leong, and K. F. Choo, "Thermal Management of Hotspots with a Microjet-Based Hybrid Heat Sink for GaN-on-Si Devices," *IEEE Trans. Components, Packag. Manuf. Technol.*, vol. 4, no. 9, pp. 1441–1450, Sep. 2014.
- [70] J. Ditri, J. Hahn, R. Cadotte, M. McNulty, and D. Luppia, "Embedded cooling of high heat flux electronics utilizing distributed microfluidic impingement jets," in *ASME 2015 International Technical Conference and Exhibition on Packaging and Integration of*

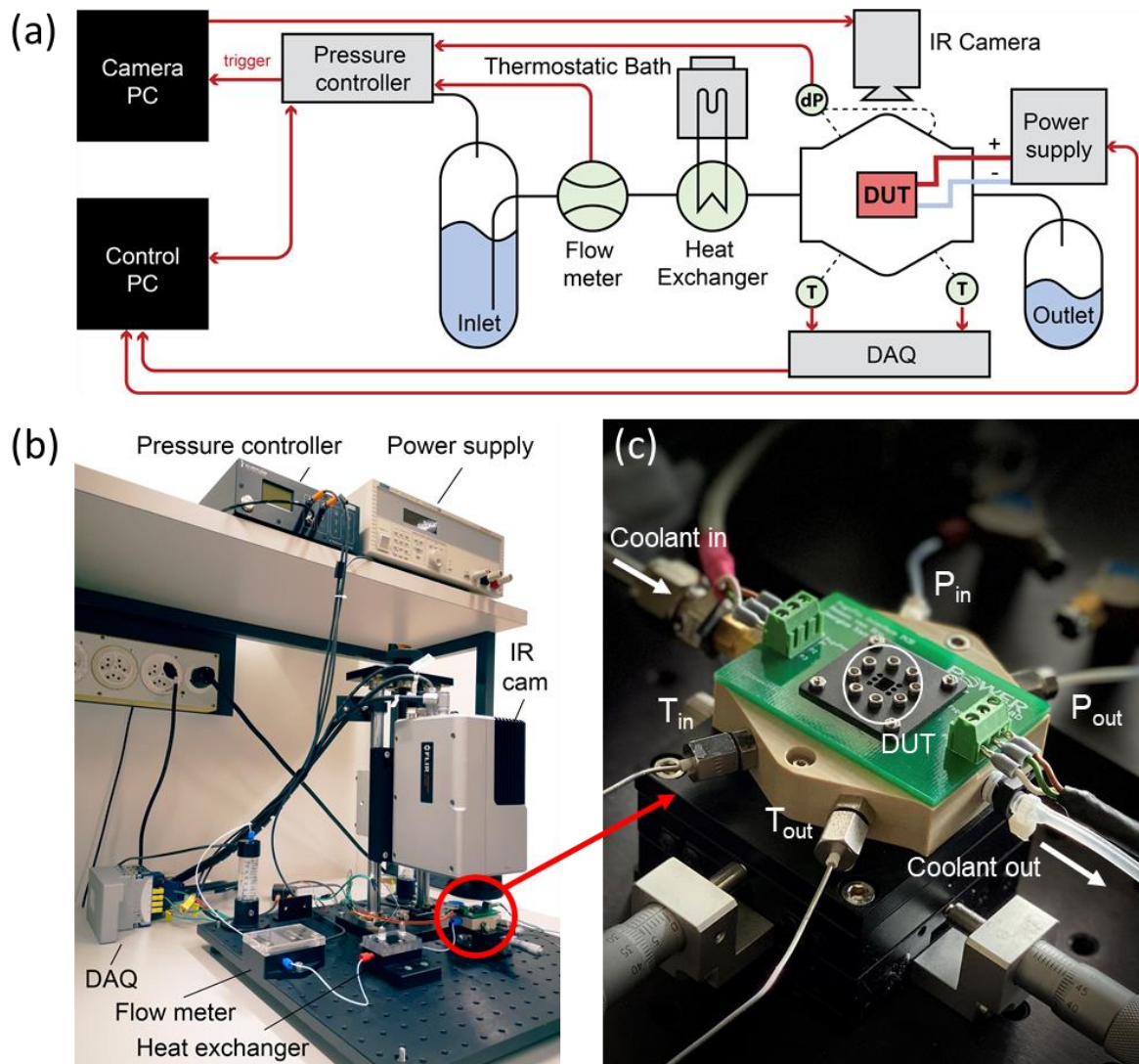
*Electronic and Photonic Microsystems, InterPACK 2015, collocated with the ASME 2015 13th International Conference on Nanochannels, Microchannels, and Minichannels*, 2015, vol. 3.

- [71] G. Natarajan and R. J. Bezama, "Microjet Cooler with Distributed Returns," *Heat Transf. Eng.*, vol. 28, no. 8–9, pp. 779–787, Aug. 2007.
- [72] T. Wei *et al.*, "High efficiency direct liquid jet impingement cooling of high power devices using a 3D-shaped polymer cooler," in *Technical Digest - International Electron Devices Meeting, IEDM*, 2018, pp. 32.5.1-32.5.4.
- [73] J. Dzuba *et al.*, "AlGaIn/GaN diaphragm-based pressure sensor with direct high performance piezoelectric transduction mechanism," *Appl. Phys. Lett.*, vol. 107, no. 12, p. 122102, 2015.
- [74] J. Ma, G. Santoruvo, P. Tandon, and E. Matioli, "Enhanced Electrical Performance and Heat Dissipation in AlGaIn/GaN Schottky Barrier Diodes Using Hybrid Tri-anode Structure," *IEEE Trans. Electron Devices*, pp. 1–6, 2016.

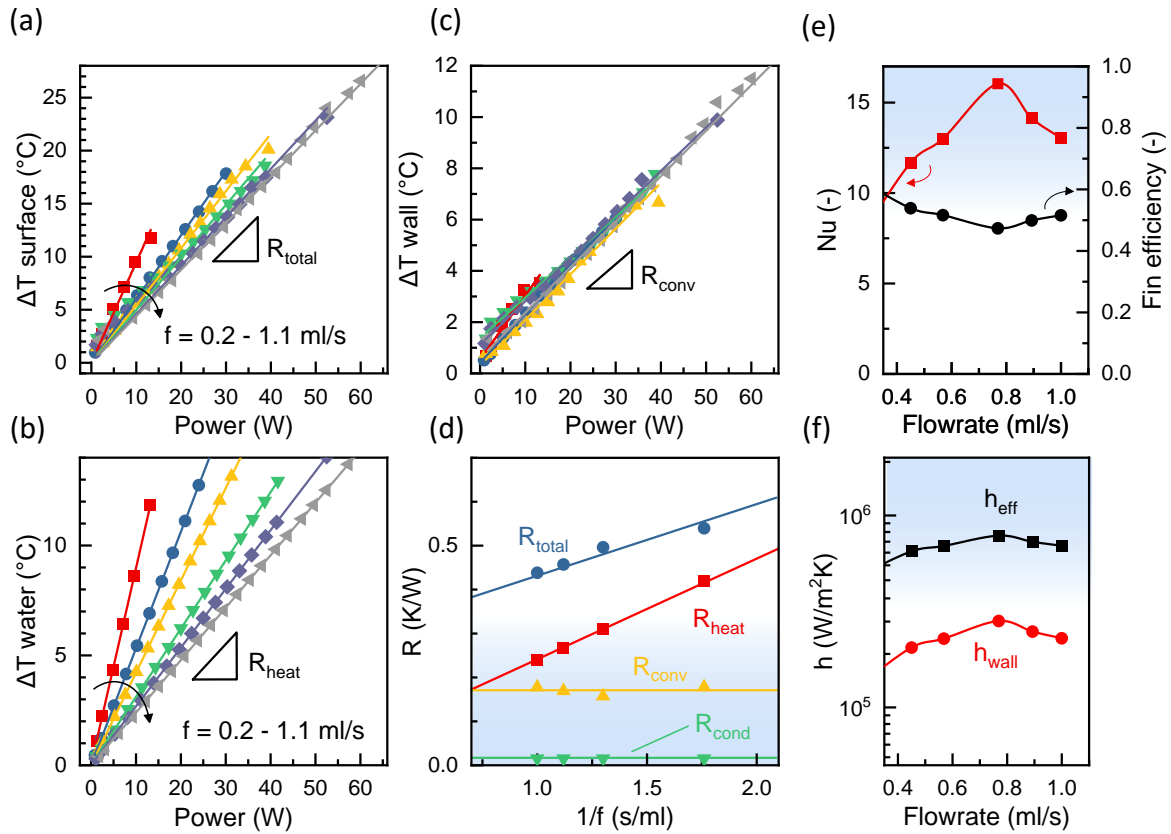
## Extended data



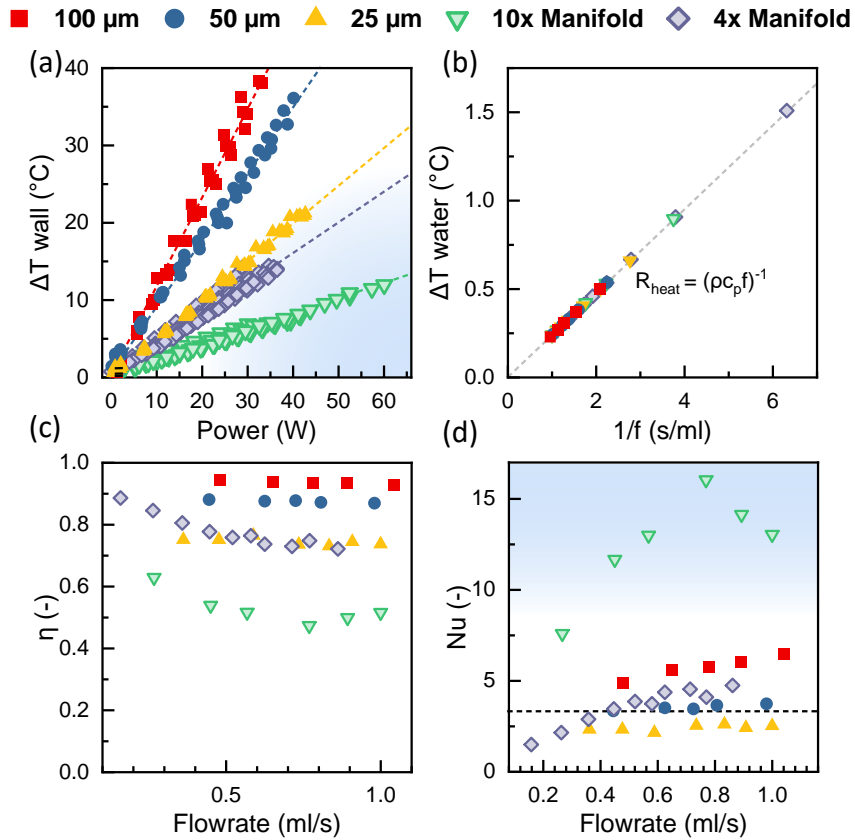
**Extended Data Fig. 1 | Fabrication process of the co-designed microfluidic-electric device. a,** AlGaIn/GaN epilayer on a silicon substrate. **b,** hard-mask deposition. **c,** Hard mask patterning and opening. **d,** Epilayer etching until reaching the substrate. **e,** anisotropic deep etching of the silicon substrate through the epilayer opening. **f,** isotropic gas etching through the epilayer opening to widen the slits under the epilayer. An in-situ optical etching tracking was put in place to control the width of the channels. **g,** Hard-mask removal. **h,** Ohmic contact deposition and annealing, seed layer deposition for electroplating and patterning the electroplating mask. **i,** Manifolds channel etching from the back of the substrate. **j,** Cr/Cu seed layer deposition for electroplating. **k,** Lithography step to define electroplating openings. **l,** Electroplating to seal the epilayer openings. **m,** Photoresist removal. **n,** Wet etch to remove Cr/Cu seed layer. **o,** Finish device fabrication with dielectric deposition, **p,** and optional gate metal deposition.



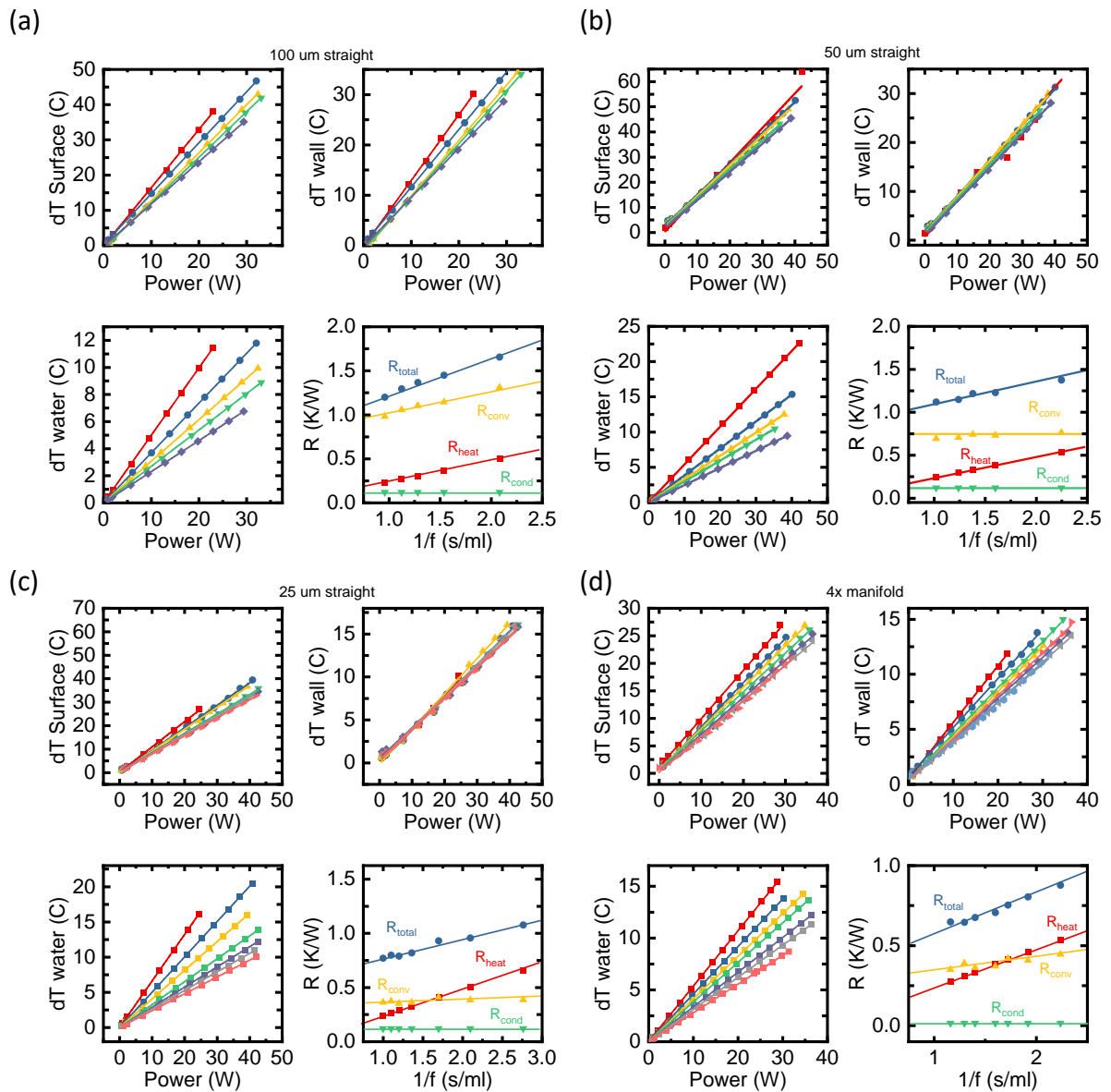
**Extended Data Fig. 2 | Experimental setup for evaluating the thermo-hydraulic performance. a,** Schematic overview of the measurement setup. An inlet reservoir of coolant is pressurized using a pressure controller, whereas the temperature is controlled using a thermostatic bath. Liquid flow through a flow-meter into the test section, containing the chip (DUT). Temperature of the chip is monitored using an IR camera, and coolant temperature is monitored using thermocouples (T). **b,** Picture of the experimental setup for characterizing the thermal performance. **c,** Close-up picture of the test section.



**Extended Data Fig. 3 | Example data reduction of thermal characterization experiments for the 10x-manifold chip.** **a**, Peak surface temperature rise above the inlet temperature, measured using IR-thermography at varying power dissipation. Slope of the linear fit through the data points gives the total thermal resistance ( $R_{\text{tot}}$ ). **b**, Wall temperature rise. Slope through these data points gives the convective thermal resistance. **c**, Water temperature rise, measured between the inlet and outlet of the chip. Slope of the linear fit through the data points gives the contribution of the total thermal resistance due to the temperature rise of the water ( $R_{\text{cal}}$ ). **d**, Total, caloric, convective and conductive thermal resistance versus the inverse flow rate. **e**, Nusselt number and fin efficiency. **f**, Effective base-area averaged heat transfer coefficient ( $h_{\text{eff}}$ ) and wall-area averaged heat transfer coefficient ( $h_{\text{wall}}$ ), taking the surface area of the microchannels as well as the fin efficiency into account.

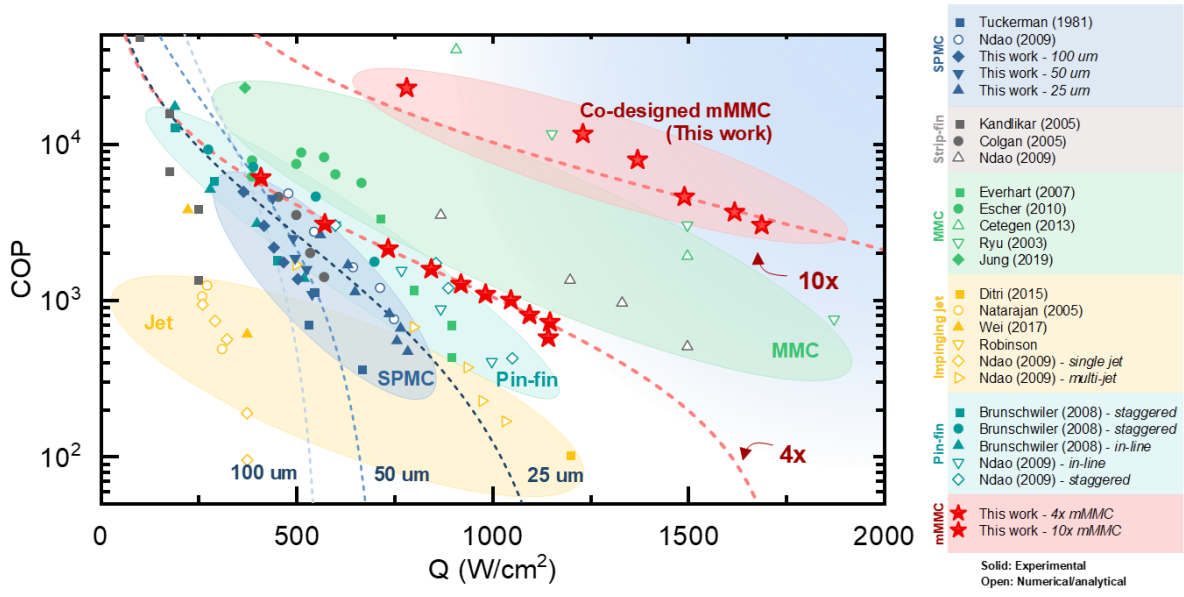


**Extended Data Fig. 4 | Overview of derived values of the thermo-hydraulic analysis.** **a**, Wall temperature for all devices. Each device shows a distinct slope in wall temperature rise versus power dissipation. **b**, Caloric thermal resistance for all evaluated flow rates, showing a clear  $(\rho c_p f)^{-1}$  relationship over all devices. **c**, Fin efficiency over a range flow rates. **d**, Nusselt number versus inverse flow rate. Dashed line indicates  $\text{Nu} = 3.66$  for fully developed internal flow.



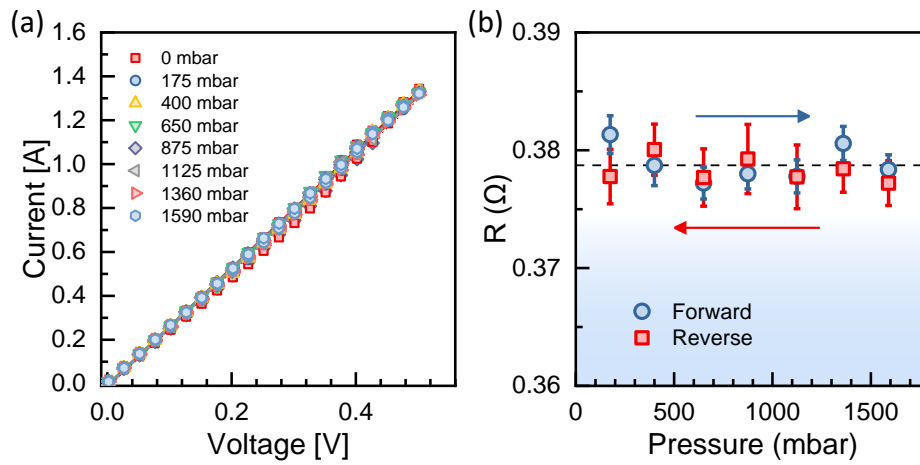
**Extended Data Fig. 5 | Additional thermo-hydraulic data.** Surface temperature rise, wall temperature rise, water temperature rise and thermal resistance for: **a**, 100  $\mu\text{m}$  straight microchannels **b**, 50  $\mu\text{m}$  straight microchannels. **c**, 25  $\mu\text{m}$  straight microchannels. **d**, 4x manifold heat sink.

**Extended Data Table 1 | Table of all design parameters and measured values per chip**

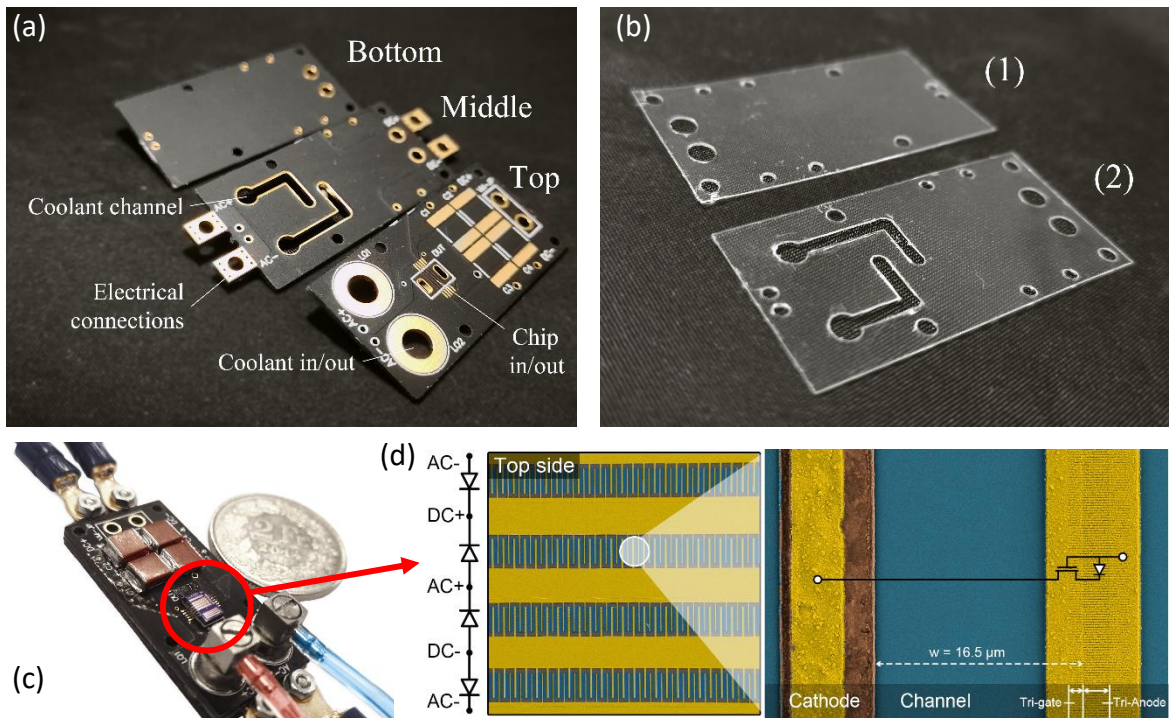


**Extended Data Fig. 6 | Extensive benchmarking plot of micro-structured cooling approaches in the literature using water as a working fluid.** COP versus heat flux for a maximum surface temperature rise of 60K. Solid markers indicate experimental results and open markers indicate numerical or analytical calculations. The results in this work are indicated by red stars. Dashed lines correspond to predictions based on a constant heat transfer. References to all used datasets can be found in Extended Data Table 2, and a tabulated data file with all used data is available in the supplementary data.

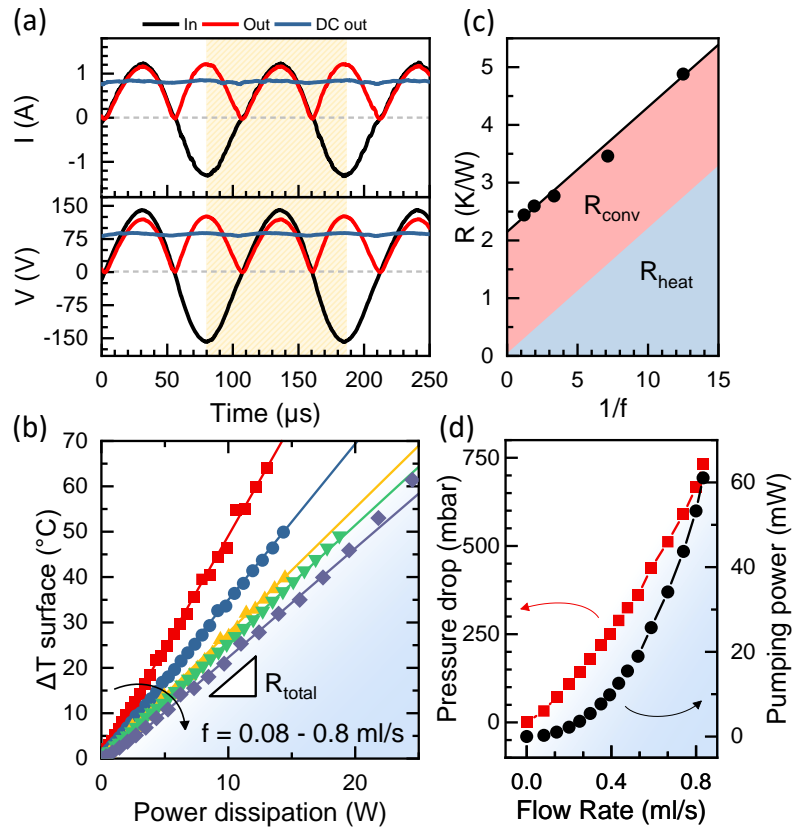
**Extended Data Table 2 | Selected references for the benchmarking study in Extended Data Fig. 6**



**Extended Data Fig. 7 | Impact of pressure on electrical performance.** **a**, IV characteristics at hydrostatic pressure between 0 mbar and 1590 mbar. **b**, Normalized change in  $R_{on}$  versus pressure during a sweep in pressure up to 1600 mbar and back. Each data point was extracted using a linear fit through a cyclic IV measurement from 0 V to 0.5 V and back.



**Extended Data Fig. 8 | Structure of the integrated full-bridge rectifier with embedded cooling.** **a**, Three PCBs that provide coolant delivery to the chip. **b**, Laser-cut adhesives used to bond the layers together. **c**, Converter after assembly, with electrical and fluidic connections. **d**, SEM image of the 4-diode structure, inset shows the polarity of each device and close up shows the structure of the tri-anode SBD diode.



**Extended Data Fig. 9 | Operation of the ac-dc converter with embedded cooling.** **a**, Input and output waveforms of 150 V / 1.2 A peak-to-peak rectification at 100 kHz. **b**, Surface temperature rise versus power dissipation for varying flow-rates. **c**, Thermal resistance versus inverse flow rate of the full converter. Pressure drop and pumping power versus flow-rate. **d**, Pressure drop and pumping power versus flow-rate.

## **Data availability statement**

All data needed to evaluate the conclusions in the paper are present in the paper, in the extended data figures and in the supplementary data